AALBORG UNIVERSITY
DENMARK

Artificial Intelligence Enabled Impedance Identification and Stability Estimation of Grid-Converter System

Zhang, Mengfan

[Link to publication from Aalborg University](#)

ARTIFICIAL INTELLIGENCE ENABLED IMPEDANCE IDENTIFICATION AND STABILITY ESTIMATION OF GRIDCONVERTER SYSTEM

BY
MENGFAN ZHANG

DISSERTATION SUBMITTED 2021

AALBORG UNIVERSITY

DENMARK

ARTIFICIAL INTELLIGENCE ENABLED IMPEDANCE IDENTIFICATION AND STABILITY ESTIMATION OF GRID-CONVERTER SYSTEM

by

Mengfan Zhang

Department of Energy Technology

Aalborg University, Denmark

.

ENGLISH SUMMARY

Moving towards a carbon-neutral society, traditional power systems are going through a shift with the wide integration of renewable energy resources, which require power-electronics-based systems as an alternative to synchronous generator systems. However, the interaction between the grid and the internal control systems of power electronics converters may result in the instability of the grid-converter system, which will threaten the security of grid operation and limit the further integration of renewables.

To address the grid-converter stability issue caused by grid-converter interaction in power converter dominated power systems, the small-signal stability analysis method that uses interface impedances is widely adopted. However, there are several issues that may undermine the performance of impedance-based stability estimation method in industrial applications. First, although the impedance modeling method is mature nowadays, some nonlinear blocks (e.g. dead-time, dc-link control loop, etc.) in the power-electronics converter are ignored, which decrease the accuracy of the impedance modeling methods and stability estimation results. Second, due to the nonlinearities in the power-electronics converter, the impedance model varies with the operating point. Thus, the impedance model obtained in a stiff operating point cannot be used for stability estimation considering the uncertainties of renewables. Moreover, many vendors are unwilling to share details of their products, making it difficult to get the full information required for impedance modeling. Therefore, to accurately estimate the stability of gird-converter system, it is significant to reveal the effect of the nonlinear block on the impedance model of power-electronics converters and to obtain the accurate impedance model in global operating point's vision without access to the detailed information of the inner control systems of converters.

To address the issues mentioned above, this Ph.D. project focuses on the converter system modeling and stability estimation and develops a series of artificial intelligence-based impedance identification methods and "black-box" stability estimation approach. The thesis consists of four research topics. First, an analytical impedance model of single-phase voltage source converter (VSC) is derived, where the dead-time effect is considered in this model with the double input describing function (DIDF) method. It is revealed that the impedance model is highly dependent on the operating point. Second, an artificial intelligence helped 'black-box' impedance identification method is developed for the impedance modeling that can cover multiple operating points. Third, to reduce the data amount requirement, a physical informed impedance identification method is developed. A combination of physics and artificial neural network (ANN) techniques is used to improve the accuracy of the impedance model with limited data. At last, an ANN-based stability estimation is developed to give a guideline on how to use the ANN-based model to achieve stability estimation.

The outcome of this thesis is expected to give a guideline of AI-based stability estimation of electrical power systems with large-scale integration of renewables, which will add significant value to the industrial applications and sustainable society.

DANSK RESUME

På vej mod det kulstofneutrale samfund gennemgår traditionelle kraftsystemer et skift med den brede integration af vedvarende energikilder, som kræver de kraftelektronikbaserede systemer som et alternativ til synkrone generatorsystemer. Imidlertid kan interaktionen mellem nettet og de interne kontrolsystemer til kraftelektronikomformere resultere i ustabilitet af net-konverteringssystem, hvilket vil true sikkerheden ved netdrift og begrænse den yderligere integration af vedvarende energi.

For at estimere gitterkonverterens stabilitetsproblem forårsaget af gitterkonverterinteraktion i strømomformerdominerede elsystemer er den lille signalanalyse, der bruger interfaceimpedanser, bredt vedtaget. Imidlertid underminerer flere problemer udførelsen af impedansbaseret stabilitetsestimering i industrielle applikationer. For det første, selvom impedansmodelleringsmetoden er moden i dag, betragtes nogle ikke-lineære blokke (f.eks. Dødtid, dc-link kontrolsløjfe osv.) I effektelektronikomformeren stadig ikke, hvilket faktisk vil påvirke nøjagtigheden af impedansmodellen og stabilitetsestimering. For det andet, på grund af ikke-lineariteterne i effektelektronikomformeren, varierer impedansen med driftspunktet, og impedansmodellen opnået i stive driftspunkter kan således ikke bruges i stabilitetsestimering i betragtning af usikkerheden ved vedvarende energi. Desuden er mange leverandører uvillige til at dele detaljer om deres produkter, hvilket gør det vanskeligt at få den fulde information, der kræves i impedansmodellering, så hvordan man aktiverer en 'sort boks' impedansmodellering og stabilitetsestimering er et nøglepunkt i industrielle applikationer. For at give et nøjagtigt skøn over stabiliteten til gordskonverteren er det vigtigt at afsløre effekten af den ikke-lineære blok i effektelektronikomformermodelleringen og opnå den nøjagtige impedansmodel i det globale driftspunktets vision uden adgang til de detaljerede oplysninger om den indre kontrolsløjfe af omformere.

For at tackle ovennævnte spørgsmål, har denne Ph.D. Projektet fokuserer på konvertersystemmodellering og stabilitetsestimering og udvikler en serie af metoden til kunstig intelligensbaseret impedansidentifikation og blackbox-stabilitetsestimering af gitterkonverteringssystemet. Specialet består af fire forskningsemner. For det første afledes en analytisk impedansmodel af enfaset spændingskildeinverter, hvor dødtidseffekten betragtes i denne model med den dobbelte indgang, der beskriver funktionsmetoden. Den genererede impedansmodel afslører, at impedansmodellen er meget afhængig af driftspunktet. For det andet er der udviklet en kunstig intelligens til 'black-box' impedansidentifikationsmetode til impedansmodellering, der kan dække flere driftspunkter. Et kunstigt neuralt netværk (ANN) -baseret multi-operations-impedansmodel oprettes ved hjælp af de målte data. For det tredje udvikles en overførselsindlæringsbaseret identifikationsmetode til at reducere datamængdekravet. En kombination af fysik og ANN-teknik bruges til at forbedre

nøjagtigheden af impedansmodellen med begrænset datamængde. Endelig udvikles et ANN-baseret stabilitetsestimat for at give en retningslinje for, hvordan man bruger den ANN-baserede model til at opnå stabilitetsestimering.

Resultatet af denne afhandling forventes at give en retningslinje for AI-baseret stabilitetsestimering af elektriske elsystemer med storskalig integration af vedvarende energi, hvilket vil tilføje betydelig værdi til de industrielle applikationer og et bæredygtigt samfund.

ACKNOWLEDGEMENTS

I am very happy to express my sincere gratitude to the all the people during the Ph.D. journey.

I would like to express gratitude to my supervisor, Prof. Xiongfei Wang. I really benefit a lot from his insightful guidance. I am also very grateful for the opportunity he gave me to cooperate with experts in other domains. I feel happy and honored that the outcome of this PhD project could add value to the practice, but I know it would not be possible without his support.

I would like to express my thanks to my assistant supervisor: Prof. Mads Græsbøll Christensen. Although we come from different research domains, I am really inspired by the discussion with him. I also would like to express my thanks to my assistant supervisor: Prof. Dongsheng Yang. I feel so lucky to be able to work with him during my first year of Ph.D. studies. Apart from the knowledge and methodology learnt from him, I am very grateful for his encouragement and support during my hard times.

Thanks and appreciation are given to Prof. Qianwen Xu and Mr. Tin Rabuzin, for the fruitful discussion during my study abroad in KTH Royal Institute of Technology. It is really inspiring to learn the challenges in the power system, especially the control and optimization of microgrids. It provides different aspects to think about how the power electronics should be. In addition, it is interesting and useful to learn how to use the Opal-RT platform.

I must express my thanks to all members in the egrid research group, especially to Donghua, Dapeng, Zheming, Heng, Yicheng and Hong, for the extensive discussion and collaboration in the research project. I would like to thank all my colleagues and staff at Aalborg University, for their kind support during my PhD studies. Special thanks to Prof. Yonghao Gui, for his warm help during my first period of my PhD journey.

Last I would like to express my deepest gratitude to my family and girlfriend for their never-ending support and understanding. They always encourage me to pursue my own dream. This Ph.D. project is supported by the Department of Energy Technique. I would like to express my grateful acknowledgement to the financial support.

Mengfan Zhang
Aalborg University, May, 2021

TABLE OF CONTENTS

TABLE OF FIGURES

TABLE OF TABLES

CHAPTER 1. INTRODUCTION

1.1. BACKGROUND AND CHALLENGES

Moving towards the carbon-neutral society, there are global trends of traditional power systems transformations with the wide integration of renewables [1], [2]. As shown in Figure 1-1, most countries have integrated renewable sources as the primary energy in 2020. Figure 1-2 shows the trends of the global share of low-carbon sources in world electricity generation between 1985 and 2020. Between 1985 and 2020, the share of renewable sources has increased from 21 % to 29 %. The trends illustrate that the installation capacity of renewables will increase in the future.

Share of renewable sources
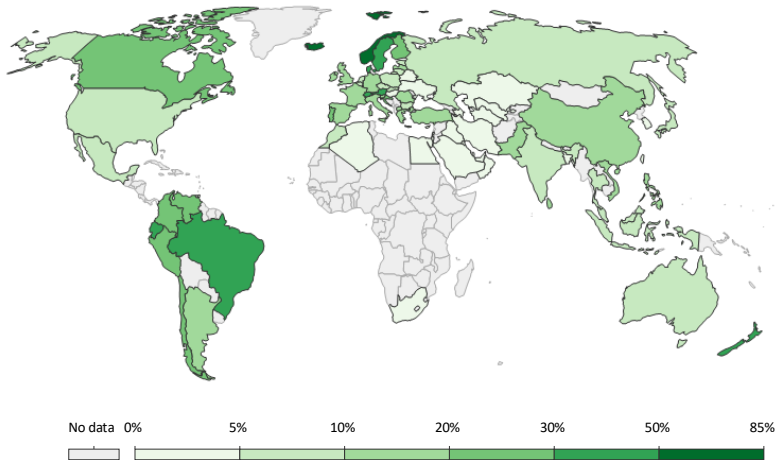
Figure 1-1. Global share of renewable sources in 2020.

Electricity production Of different sources
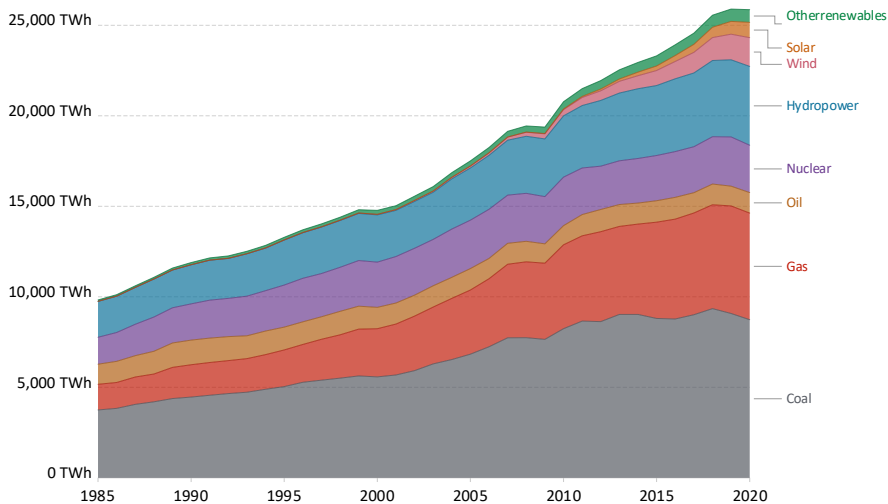
Figure 1-2. Trends of electricity production by source between 1985 and 2020.

Power-electronics converters, which serve as the connection between the grid and the renewables, gradually replace the synchronous generators as the major sources of the power system. As the trend continues, conventional synchronous generators dominated power systems are evaluating to the next-generation power systems, which are known as power electronics dominated power systems in the future. The power electronics dominated power system enables the high penetration of renewables and fully controllable power converters, which makes the grid more sustainable and flexible.

However, different from synchronous generators, high-dynamic power converters cannot provide enough inertia to keep the system stable [3], [4]. The interaction between the grid and the internal control systems of power electronics converters may result in the instability of grid-converter systems, which will threaten the security of grid operation and limit the further integration of renewables. In addition, renewable energy sources are highly weather-dependent and intermittent, which introduce the uncertainties of generated power. Thus, the stability of the power electronics dominated power system cannot be predicted using the traditional power system stability analysis method, where only the fixed operating points are considered. Hence, it is necessary to deliver an advanced modeling method, which can fill the research gap of existing modeling and analysis for power electronics dominated power system and develop a corresponding stability analysis framework for the grid-converter interaction system considering the dynamics of the power electronics

converter and the uncertainties of renewable energy sources based on the proposed modeling method.

1.2. OBJECTIVES AND MOTIVATION

1.2.1. STATE-OF-ART

1.2.1.1 Modeling of power electronics converter

To give an accurate stability estimation of the grid-converter interaction system, it is of vital importance to gain an accurate model of the system considering the dynamics of the power electronics converter and the uncertainties of renewable energy sources.

The modeling methods are divided into theoretical modeling and behavioral modeling [5]-[9]. For the theoretical modeling method, the model is usually derived based on the physical principles. The derived theoretical model has a clear physical interpretation. While for behavioral modeling methods, the models are generated through the measurement data with identification techniques, and there is no need to get prior knowledge of the detailed system [10]-[12].

For the theoretical modeling method of power electronics converters, the most important and fundamental method, named average modeling, was first proposed in 1972 by R. D. Middlebrook [13]-[14]. The power electronics converters could be represented with a time-invariant continuous equivalent circuit based on the average modeling method. On the basis of the theory, different modeling methods are proposed for different purposes. For the stability analysis of the grid–converter system, the most popular modeling methods are the impedance-based modeling approach and state-space modeling approach [15]-[17].

1.2.1.2 Stability analysis of gird-converter system

To analyze the stability of the grid–converter system, different methods have been proposed in previous literatures. For the state-space model based stability analysis, the eigenvalues of the system matrix could provide a complete view of the system oscillation, while the participation analysis could reveal the relationship between the system dynamics and the state variables [18]. Thus this method can reveal the root causes of instability of the interaction systems [19].

Although the state-space model has the advantage in the global view of the system dynamics, it shows the complexity and less scalability when analyzing the large-scale interconnected systems with the coupled-dynamics of different control loops [20]. To overcome the disadvantages, the impedance-based stability analysis has been proposed [21]-[23]. The converters with the linear control loop are modeled as single-input single-output (SISO) transfer functions. The SISO impedances of the converter

and the grid impedance could be used for the stability analysis with the bode plot or Nyquist criterion [24]. And for the converters with the nonlinear control loops, the output impedance model should be modeled as the multiple-input multiple-output (MIMO) impedance model [25]. With the help of generalized Nyquist criterion, the stability condition could be assessed. If each power electronics converter in the interconnected system could be modeled as the impedance model, it is of much ease to obtain the stability condition of the system. Meanwhile, there is no need to model the whole system again if the extra power converters are added or removed from the system, which shows good scalability.

1.2.1.3 Research gaps

Although the impedance-based stability analysis is widely adopted, several issues undermine the performance of impedance-based stability estimation in industrial applications.

First, although the impedance modeling method is mature nowadays, some nonlinear blocks (e.g. dead-time, dc-link control loop, etc.) in the power-electronics converter are still not considered, which will affect the accuracy of the impedance model and the stability estimation. Dead-time is such a nonlinear block for the VSC to reject the shoot-through during the converter operation, but also changes the dynamic behavior of the VSCs [26]. In previous literature, the dead-time is viewed as an external disturbance of the converter and analyzed by Fourier decomposition [27-30]. As reported in [31-32], the dead-time effect is modeled as a small-signal model. The sign function is adopted to reveal the voltage-loss phenomenon caused by the dead-time, with the help of Fourier decomposition, the sign function is linearized with its fundamental component. However, due to the neglect of the current ripple, the model cannot reveal the dead-time effect. To address this issue, the describing function is proposed to establish the model [33]. However, only the fundamental component of linearization is considered in this work.

Second, due to the nonlinearities in the power-electronics converter, the impedance varies with the operating point, thus the impedance model achieved in a stiff operating point cannot be used in stability estimation considering the uncertainties of renewables. To address this issue, as reported in [34], a modeling method is proposed, where the function of the disturbance signal is integrated into the impedance model to represent the variation of the operating point. Hence, the large-signal impedance model is generated. Another method is to employ the polytopic model for converter modeling at different operating points, which can be seen as a 'black-box' small-signal model [35-36]. The small-signal models at different operating points are summarized with respective weights to generate the multi-operating-point (MOP) model. The generated model can predict the impedance at different operating points, yet this model can just predict the model of the converters at limited operating points and the accuracy is hard to be guaranteed.

Third, many vendors are unwilling to share details of their products, making it difficult to get the full information required in impedance modeling, then how to enable a 'black-box' impedance modeling and stability estimation is a key point in industrial applications. To overcome this challenge, the impedance measurement is developed to directly obtain the impedance by measurement and frequency scanning without the prior information of inner control systems and enables the 'black-box' stability estimation [37-38]. However, the existing impedance measurement-based stability analysis methods are conducted only at the stiff operating scenario, and cannot deal with continuous variations. Due to the fluctuations of renewables and loads, the operating point of the grid-converter system varies consistently. Thus, the impedance model of the converter is variable when connecting to renewables, making it challenging to be estimated by conventional impedance measurement methods. Meanwhile, since the operating points are the high-dimension vector, it is unrealistic to measure enough data through the online impedance identification, as the limited measured data amount will consequently introduce the over-fitting phenomena to the trained impedance model, and then affect the accuracy of stability analysis [39].

Therefore, to give an accurate estimation of gird-converter stability, it is significant to reveal the effect of the nonlinear block in the power-electronics converters modeling and obtain the accurate impedance model in the global operating point's vision without access to the detailed information of the inner control loop of inverters.

1.2.2. OBJECTIVES

To fill in the identified research gap, the objectives of the thesis are summarized as:

- To obtain an accurate analytical model considering the dead-time effect.

- To obtain the 'black-box' impedance model of the VSC covering the variable operating points with the help of AI.

- To develop a physical aware impedance identification method that reduces the data amount requirement in real industrial applications.

- To adopt the AI technique to achieve the stability analysis of the grid-converter system.

1.3. MAJOR CONTRIBUTIONS

The contributions of the thesis are summarized below:

- The Ph.D. thesis presents the accurate small-signal model for VSCs considering the dead-time effect. The current ripple of VSC is analyzed for

a more accurate model of dead-time effect. The DIDF method is employed for nonlinear modeling caused by dead-time effect. The presented impedance model could accurately help for the controller design of VSC and stability analysis of the grid-converter system.

• The Ph.D. thesis develops a 'black-box' ANN-based impedance identification method for VSC impedance modeling. A methodology adopting the ANN technique for the VSC modeling is illustrated, which could be used for the stability analysis of the modern power electronics based power systems considering the increasing integration of renewables.

• The Ph.D. thesis develops a physical aware impedance identification method that reduces the data amount requirement for online impedance identification. Considering the data limitation in online impedance measurement, the physical informed transfer learning based impedance identification is developed for online impedance identification effectively.

• The Ph.D. thesis develops a double deep neural network (DNN) based black-box modeling and stability region estimation method, which consists of a DNN based MOP-impedance model and a DNN-based stability discrimination model. The stability region of the grid-converter system can be accurately predicted by the proposed approach.

1.4. THESIS LAYOUT

The origination of the thesis is list below:

Chapter 1 introduces the ongoing trend of traditional power system transformations towards the power electronics-based power system. Following this trend, more and more renewables are integrated into the power system with the connection of the power electronics converters, which may result in instability issues.

Chapter 2 discusses the modeling of the dead-time effect, which is necessary for inverter operation and has a significant effect on the output impedance of inverters. The double input describing function method is adopted to describe such effects on the analytical impedance model.

Chapter 3 proposes a data-driven modeling method for VSC. The AI technique is adopted to model the power-electronics converters. The ANN-based impedance identification method is proposed to identify the MOP-impedance model of VSCs. First, the impedance measurement is adopted to acquire the impedance data of VSCs. Second, the measured data are fed into the ANN model to train the MOP-impedance

model of VSCs, which can predict impedance models at the unmeasured operating points.

Chapter 4 discusses the data amount limitation issues in real industrial applications. A framework of the physics informed neural network based online impedance identification of VSC is established to illustrate the detailed implementation of the proposed method.

Chapter 5 tackles the challenge of how to estimate the stability region considering the uncertainties of the renewables. In this chapter, a double deep neural network (DNN) based black-box modeling and stability region estimation approach for power converter dominated power systems is proposed. The proposed double DNN based framework achieves fast and accurate estimation of stability region for grid-converter system considering the variation of the operating point.

Chapter 6 illustrates the conclusion and the future work.

Figure 1-3 shows the framework of the thesis.
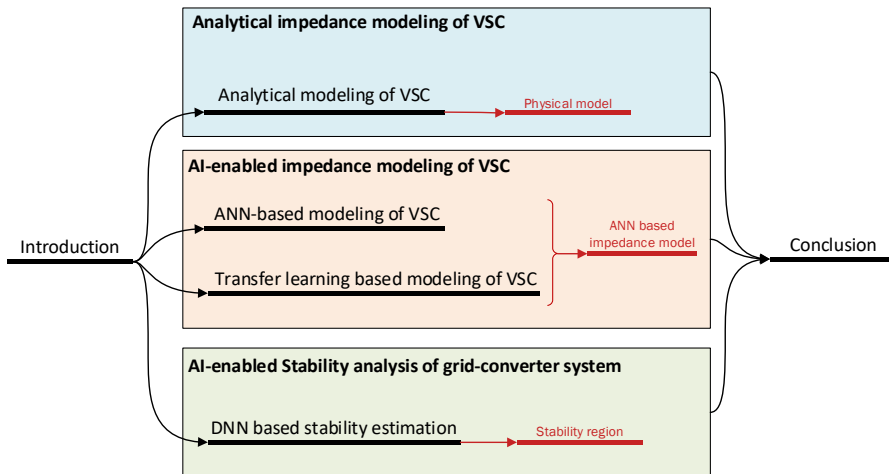
Figure 1-3. Thesis framework.

1.5. LIST OF PUBLICATIONS

The relationship between the chapter number and published papers is given by.

Chapter No.	Related Publications
2	C1
3	J1
4	J2, C2
5	J3

Journal paper:

J1 **M. Zhang**, X. Wang, D. Yang and M. G. Christensen, "Artificial Neural Network based Identification of Multi-Operating-Point Impedance Model," *IEEE Trans. Power Electron.*, vol. 36, no. 2, pp. 1231-1235, Feb. 2021.

J2 **M. Zhang**, X. Wang, Q. Xu and M. G. Christensen "Transfer Learning based Impedance Identification of Voltage Source Converters," submitted to *IEEE Trans. Power Electron*.

(This paper is pre-print in TechRxiv: https://doi.org/10.36227/techrxiv.14568954.v1)

J3 **M. Zhang**, X. Wang and Q. Xu, "Deep Neural Network based Black-Box Stability Region Estimation of Grid-Converter Interactions," submitted to *IEEE Trans. Ind. Electron*.

Conference paper:

C1 **M. Zhang**, D. Yang, and X. Wang, "Accurate open-loop impedance model of single-phase voltage source inverter (VSI) considering the dead-time effects," in *Proc. 20th Workshop Control Modeling Power Electron*. (COMPEL), Toronto, ON, Canada, Jun. 2019, pp. 1–5.

C2 **M. Zhang**, X. Wang, D. Yang, Z. Cui and M. G. Christensen, "Transfer Learning for Identifying Impedance Estimation in Voltage Source Inverters," in *Proc. IEEE Energy Convers. Congr. Expo*. (ECCE), Oct. 2020, pp. 6170-6174.

C3 **M. Zhang**, X. Wang and Q. Xu, "Data-Driven Modeling of Power-Electronics-Based Power Systems Considering the Operating Points Variation," in *Proc. IEEE Energy Convers. Congr. Expo*. (ECCE), Oct. 2021, accepted.

CHAPTER 2. ANALYTICAL MODELING OF VSC CONSIDERING DEAD-TIME EFFECT

The chapter is based on **C1**.

2.1. BACKGROUND

The impedance-based stability analysis method is widely used for VSC-grid interaction stability analysis. For this reason, the accuracy of the impedance model is vitally important. Yet, there are few studies on nonlinearities of the VSC, which affect the accuracy of modeling of VSC impedance and the stability analysis of the VSC-grid interaction system [40].

Dead-time is such a nonlinear block for the VSC to reject the shoot-through during the converter operation, but also changes the dynamic behavior of the VSCs . The double input describing function (DIDF) based modeling method is proposed to accurately model the dead-time effect.

This chapter is organized as: In Section 2.2, the DIDF basics is introduced. In Section 2.3, the proposed DIDF method is employed to model the VSC with the dead-time block. In Section 2.4, both the simulation and the experiment are adopted to validate the derived impedance models.

2.2. DUAL INPUT DESCRIBING FUNCTION BASICS

For an arbitrary function $y = f(x)$, suppose the input is a sinusoid function, the function $f[Msin(\omega t)]$ is represented as the summation of sinusoidal functions. The describing function $N(M)$ is

$$N(M) = \frac{1}{M}\left(a_f + b_f\right) \tag{2.1}$$

$$\begin{cases} a_f = +\dfrac{1}{\pi} \cdot \displaystyle\int_0^{2\pi} f(M \cdot \sin \omega t) \cdot \sin \omega t\, d\omega t \\[2mm] b_f = -\dfrac{1}{\pi} \cdot \displaystyle\int_0^{2\pi} f(M \cdot \sin \omega t) \cdot \cos \omega t\, d\omega t \end{cases} \tag{2.2}$$

Therefore, the function $f(x)$ with the sinusoid input can be represented in this format $y = N(M)\, x$.

However, in the modeling of dead-time effect, the nonlinear input is composed of two additive sinusoids, i.e., the fundamental wave and small-signal perturbation. For the purpose of calculation, the function $f(x)$ is assumed as

$$f(t) = O \cdot \sin(\omega_O t + \theta_O) + P \cdot \sin(\omega_P t + \theta_P) \tag{2.3}$$

where the amplitudes O and P and angular frequencies ω_O and ω_P are determined by the system nature, the randomness of the inputs is determined by the phase angles θ_O and θ_P.

In this case, only the phase angle of the sinusoid function is the random variable, the other phase angle is related to it. The describing functions are determined by the relation between the fundamental wave and small-signal perturbation, which is written as follow

$$N(O) = \frac{M_O}{I_O}, N(P) = \frac{M_P}{I_P} \tag{2.4}$$

where M_O, I_O, M_P and I_P are the phasor of output and input of the fundamental wave and small-signal perturbation, respectively.

If the nonlinearity of the function $y = f(x)$ is static, the describing functions of the dual inputs are written as follow

$$\begin{aligned}
N(O) &= \frac{1}{2\pi^2 O} \int_0^{2\pi} d\theta_O \int_0^{2\pi} d\theta_P f\left(O \cdot \sin\theta_O + P \cdot \sin\theta_P\right) \sin\theta_O \\
N(P) &= \frac{1}{2\pi^2 P} \int_0^{2\pi} d\theta_O \int_0^{2\pi} d\theta_P f\left(O \cdot \sin\theta_O + P \cdot \sin\theta_P\right) \sin\theta_P
\end{aligned} \tag{2.5}$$

The DIDF of the nonlinear function only depends on the amplitude of the inputs.

2.3. **DEAD-TIME MODELING BY DIDF**
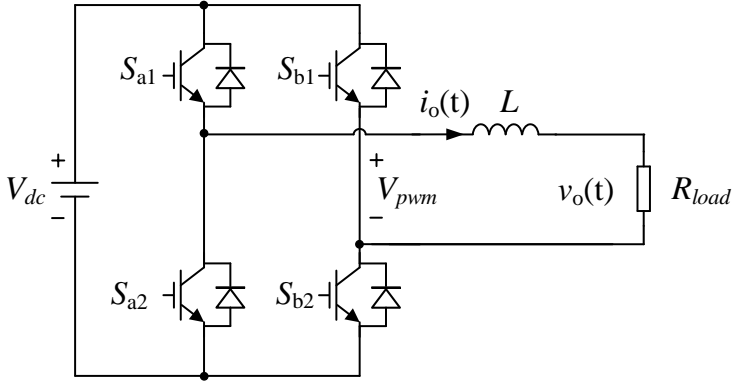
Figure 2-1. Diagram of single phase VSC.

The single phase VSC is shown in Figure 2-1. V_{dc} is the dc voltage. L is the filter inductance. S_{a1}, S_{a2}, S_{b1} and S_{b2} are the switches. $i_o(t)$ and $v_o(t)$ are the current and load voltage of the VSC system, respectively, V_{pwm} is the bridge voltage of VSC. The model of converter can be easily written as:

$$L\frac{di_o(t)}{dt} + v_o(t) = V_{pwm} = d \cdot V_{dc} \tag{2.6}$$

where d denotes the VSC duty ratio.

Due to the dead-time effect, the duty ratio will be changed. Figure 2-2 shows the VSC current, which consists of three periods, the red part is the positive period, the yellow part is the zero-crossing period and the blue part is the negative period.
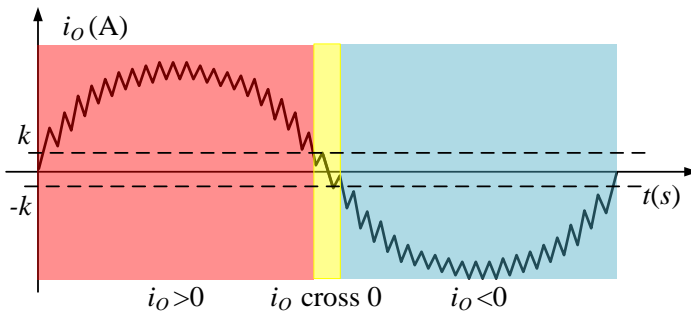
Figure 2-2. Output current considering current ripple.

In the normal period, the duty ratio does not change. But in the dead-time period, the paralleled freewheeling diodes are affected by the inductor current, which will change the actual duty ratio in the period of dead-time. Figure 2-3 shows the dead-time effect in the dead-time period with different situations of the output current. T_{sw} is the switching period, V_{pwm} and $V_{pwm,act}$ are the ideal output voltage of VSC and the actual VSC voltage, $S_{a1,id}$, $S_{a1,id}$, $S_{a1,act}$ and $S_{a1,act}$ are the ideal and actual switches.

As shown in Figure 2-3, when $i_o > 0$, the actual output voltage $V_{pwm,act}$ caused by dead-time effect is less than the ideal VSC voltage V_{pwm}. When $i_o < 0$, the actual conduction time of VSC is larger than the ideal conduction time. When i_o crosses zero, the actual conduction time of VSC is equal to the ideal conduction time and the dead-time has no effect. Thus, this dead-time effect of VSC is modeled as the function below

$$d_{act} = d_{idea} - \frac{T_{dead}}{T_{sw}} \cdot f\left(i_o\left(t\right)\right) \tag{2.7}$$
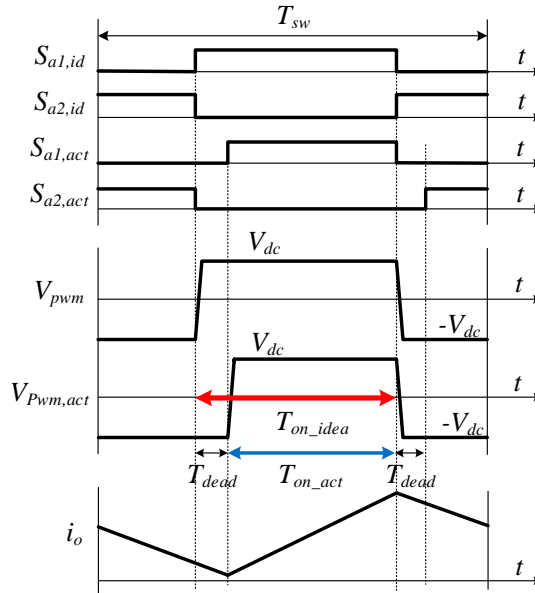
a). $i_o < 0$.
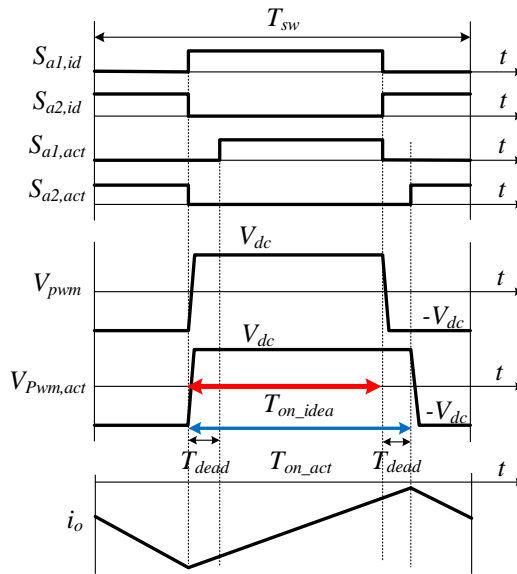
b). $i_o < 0$.
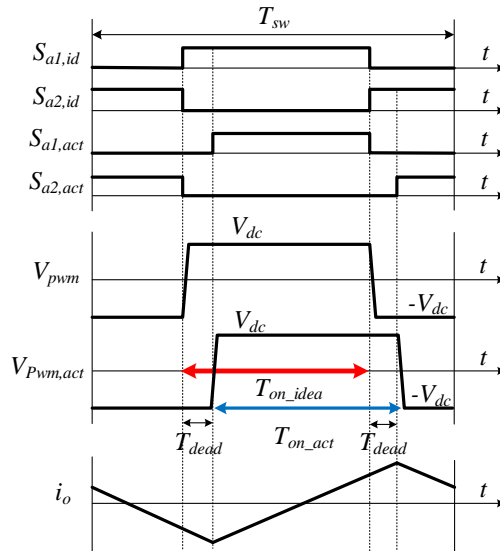
c). i_o crosses 0.

Figure 2-3. Dead time effect with different inductor current.

where

$$f\left(i_o\left(t\right)\right)=\begin{cases}1, & i_o\left(t\right)\geq tr \\ 0, & tr>i_o\left(t\right)>-tr \\ -1, & i_o\left(t\right)\leq -tr\end{cases} \quad (2.8)$$

Where tr is the threshold of the current, which is shown in Figure 2-2, which can be calculated as follow

$$tr=\Delta i_O=\frac{T_{sw}\cdot V_{dc}}{2L} \quad (2.9)$$

Substituting (2.9) into (2.6), the VSC considering the dead-time effect is given as

$$L\frac{di_o\left(t\right)}{dt}+v_o\left(t\right)=V_{dc}\cdot\left(d_{idea}-\frac{T_{dead}}{T_{sw}}\cdot f\left(i_o\left(t\right)\right)\right) \quad (2.10)$$

Then, the small-signal perturbation is added into (2.10) as shown below

$$L\frac{d\left(i_p\left(t\right)+i_s\left(t\right)\right)}{dt}+v_p\left(t\right)+v_s\left(t\right)=\left(d_{idea}-\frac{T_{dead}}{T_{sw}}\cdot f\left(i_p\left(t\right)+i_s\left(t\right)\right)\right)\cdot V_{dc} \quad (2.11)$$

where the subscript s represents the steady state signal and p represents the small-signal perturbation. As the function $i_s(t)$ and $i_p(t)$ in this case are sinusoids, then the Fourier series of the function is represented with the DIDF

$$f\left(I_s\cdot\sin\omega_s t+I_p\cdot\sin\left(\omega_p t+\varphi\right)\right)$$
$$=\sum_{m=0}^{\infty}\sum_{n=\begin{cases}-\infty(m\neq 0)\\0(m=0)\end{cases}}^{\infty}[P_{mn}\sin\left(m\psi_1+n\psi_2\right)+Q_{mn}\cos\left(m\psi_1+n\psi_2\right)] \quad (2.12)$$

where $\psi_1=\omega_s t$, $\psi_2=\omega_p t+\varphi$ represent two arbitrary angles. By the describing function theory mention in last section, the DIDF of $f(i_s(t)+i_p(t))$ are obtained as below

$$f\left(I_s\cdot\sin\omega_s t+I_p\cdot\sin\left(\omega_p t+\varphi\right)\right)\approx N_s\cdot i_s+N_p\cdot i_p \quad (2.13)$$

$$N_S=\frac{P_{10}}{I_s}=\frac{1}{2\pi^2 I_s}\iint_\Omega f\left(I_s\cdot\sin\psi_1+I_P\cdot\sin\psi_2\right)\sin\left(\psi_1\right)d\psi_1 d\psi_2$$
$$N_P=\frac{P_{01}}{I_p}=\frac{1}{2\pi^2 I_P}\iint_\Omega f\left(I_s\cdot\sin\psi_1+I_P\cdot\sin\psi_2\right)\sin\left(\psi_2\right)d\psi_1 d\psi_2 \quad (2.14)$$

Substituting (2.8) into (2.14), the describing function of the $f(i_s(t) + i_p(t))$ can be derived

$$N_P = \frac{4}{\pi I_s} \cdot \sqrt{1 - \left(\frac{k}{I_s}\right)^2} \cdot \sum_{n=0}^{\infty} \left[\frac{(2n)!}{2^{2n} n!^2}\right]^2 \frac{1}{1-2n} \left(\frac{I_p}{I_s}\right)^{2n}$$

$$N_S = \frac{4}{\pi I_s} \cdot \sqrt{1 - \left(\frac{k}{I_s}\right)^2} \cdot \sum_{n=0}^{\infty} \left[\frac{(2n)!}{2^{2n} n!^2}\right]^2 \left(\frac{I_p}{I_s}\right)^{2n}$$

$$(2.15)$$

Substituting (2.15) into (2.10) and (2.13), the state-space model of VSC is obtained

$$\frac{d\left(i_s(t) + i_p(t)\right)}{dt}$$
$$= \frac{1}{L}\left(\left(d_{idea} - \frac{T_{dead}}{T_{sw}} \cdot \left(N_s \cdot i_s(t) + N_p \cdot i_p(t)\right)\right) \cdot V_{dc} - \left(v_s(t) + v_p(t)\right)\right)$$

$$(2.16)$$

Eliminate the steady states of the equation (2.16), the small-signal VSC model is obtained

$$\frac{di(t)}{dt} = \frac{1}{L}\left[\left(d_{idea} - \frac{T_{dead}}{T_{sw}} \cdot N_p \cdot i(t)\right) \cdot V_{dc} - v(t)\right]$$

$$(2.17)$$

2.4. CASE STUDY

Figure 2-4 shows the diagram of the single phase VSC. In the case study setup, the impedances are obtained from the simulation using the frequency scanning impedance measurement technique [41]. The current perturbation is injected into the system. The output voltage and current waveforms at the point of common coupling (PCC) are recorded. Then the Fast Fourier Transform (FFT) algorithm is adopted to filter out the corresponding frequency current and voltage at the frequency domain. Frequency scanning technology is adopted for the impedance curve at the whole interested frequency range. As a reference, the analytical impedance model is

$$Z_{ol} = L \cdot s + V_{dc} \cdot \frac{T_{dead}}{T_{sw}} \cdot \sqrt{1 - \left(\frac{k}{I_{op}}\right)^2} \cdot \frac{4}{\pi \cdot I_{op}}$$

$$(2.18)$$

where I_{op} represents the peak value of output current.
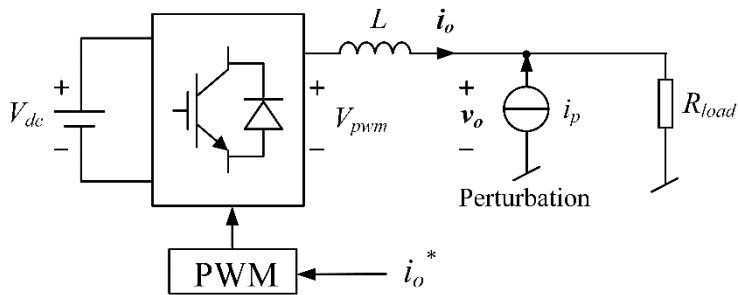
Figure 2-4. System diagram of open-loop VSC.

The simulation parameters are shown in *Table 2-1*.

V_{dc} [V]	L [mH]	I_{op} [A]	T_{sw} [μs]	T_{dead} [μs]
700	8	5.4	100	4

Table 2-1 Parameters of simulation setup.

The proposed impedance model results in Figure 2-5 shows a good matching with the simulation results. To show the advantage of the proposed method compared with impedance derived with the conventional method, the conventional impedance model is also shown in Figure 2-5. As the result shows, the proposed model can accurately model the dead-time effect.

A 1 kW experiment is designed to validate the proposed model. Figure 2-6 shows the experimental setup. One inverter is the under-test inverter, while another serves as the perturbation source. The current sensor and the voltage sensor are used to measure the voltage and current responses at the PCC. The sampled voltage and current are processed with the FFT algorithm. By sweeping the frequency, the impedance curve of VSC is generated.

The parameters of the experiment are kept the same as the simulation.
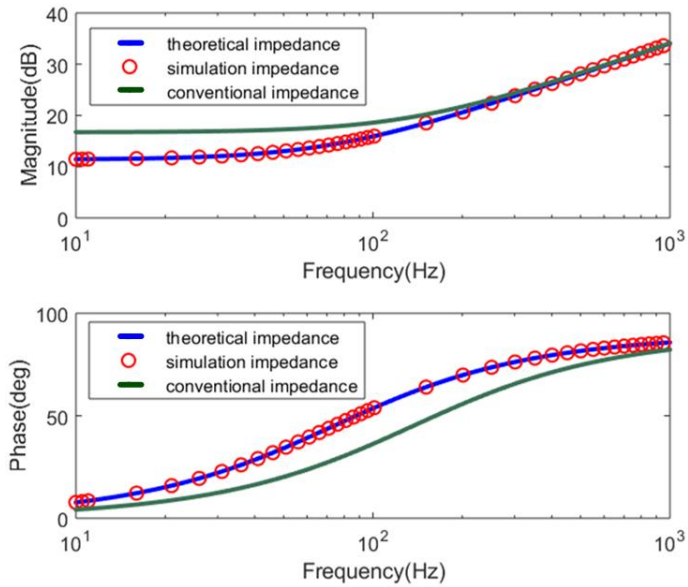
Figure 2-5. Simulation comparison between measured impedance data and proposed model.
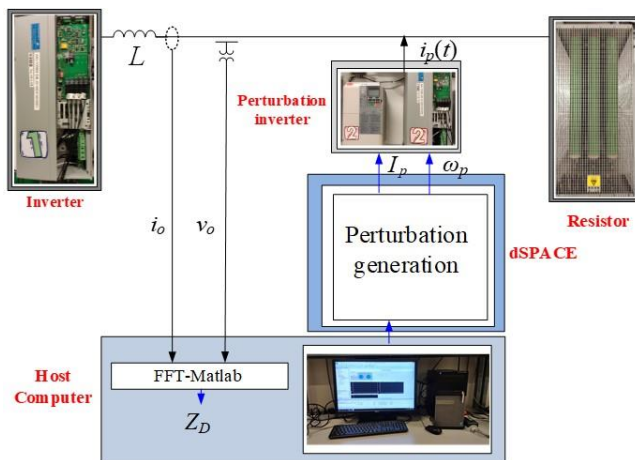
Figure 2-6. Diagram of the experiment of impedance measurement.

The comparison experiment result is shown in Figure 2-7, which compares the actual measured impedance, the small-signal model derived with the proposed modeling method and the impedance model with the conventional method. As shown in Figure

2-7, the proposed impedance model measured matches well with impedance and is more accurate than the conventional one.
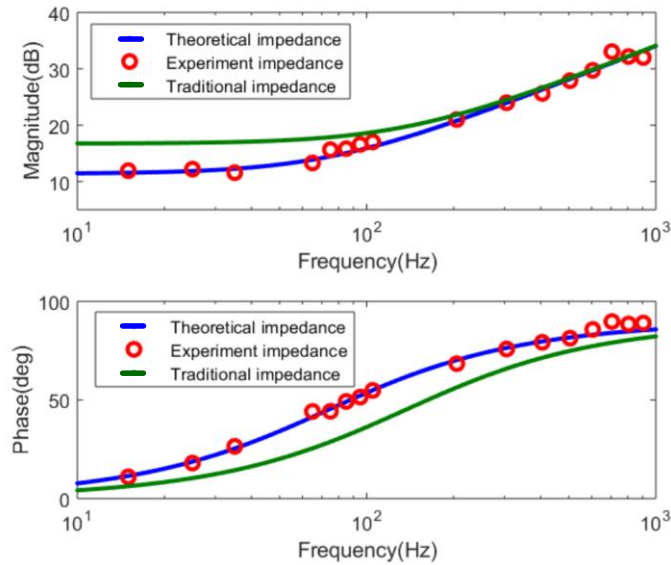
Figure 2-7. Experimental comparison between measured impedance data and proposed model.

2.5. SUMMARY

The accurate small-signal model for VSCs considering the dead-time effect is developed in this chapter. The current ripple of VSC is analyzed for a more accurate model of dead-time effect. The DIDF method is employed in this chapter for nonlinear modeling of the dead-time. Both the simulation and the experiment are conducted to validate the proposed model.

CHAPTER 3. DATA-DRIVEN MODELING OF VSC

The chapter is based on **J1**.

3.1. BACKGROUND

The VSC impedance is highly relative to the operating point, due to the nonlinearity of VSC control systems [42]. Hence, it is hard to give the stability estimation of the VSC-grid system with the impedance at a fixed operating point.

To address this issue, in this chapter an ANN-based impedance identification method is proposed to identify the MOP impedance model of VSCs. First, the impedance measurement is adopted to acquire the impedance data of VSCs. Second, the data are fed into the ANN model to train the MOP-impedance model of VSCs, which can predict the impedance. At last, the comparison results are provided to validate the proposed method.

3.2. FRAMEWORK OF PROPOSED METHOD

ANN can directly use the data to train the impedance model by mimicking the structure of a biological neural network.

Figure 3-1 shows the framework of the proposed ANN-based impedance identification. This framework gives an illustration of how to adopt the ANN technique in impedance identification. As shown in Figure 3-1, the framework consists of three levels.

At the concept level, the framework illustrates how to generate the model from data and how to validate the model in the deep learning domain.

At the mapping level, the framework bridges the research gap between the machine learning domain and the power electronics domain. In the data sourcing part, the impedance data at different operating points are measured. First, the interval and range of the sweeping parameter are defined before the measurement. Second, the impedance measurement is used to acquire the impedance data with changing operating points. The ANN model training technique is used to train the MOP-impedance model of VSCs considering the continuous changing of operating points. In the model validation part, the accuracy of the generated model is verified by comparing the predictive impedance with the model and the field measured data.

The supporting level consists of two supportive techniques for the mapping level. The impedance measurement is adopted for the impedance data generation, and the ANN training is used for the model generation [43]. The implementation is illustrated in the next section.
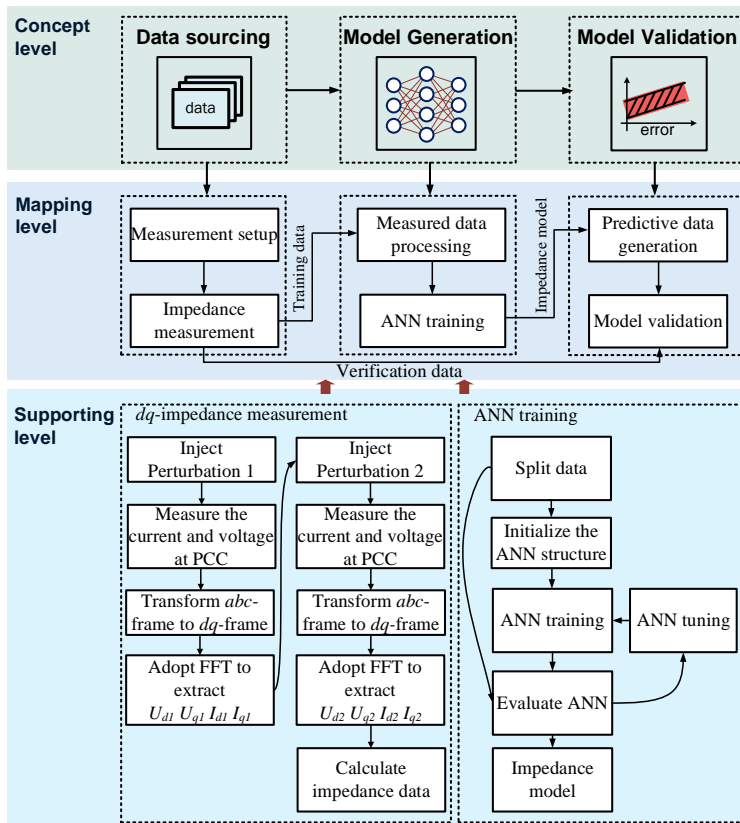
Figure 3-1 Proposed ANN-based impedance identification framework.

3.3. IMPEDANCE MEASUREMENT

The frequency scanning impedance measurement is used to acquire the dataset for model training.

Figure 3-1 shows the workflow of the online impedance measurement.

First, the perturbation signal is appropriately designed to be designed before the measurement [44]. If the magnitude is not small enough, the operating point of the VSC will be changed. Meanwhile, if it is not sufficiently large, the noise disturbances

will affect the measurement. According to [45], [46], the perturbation is set to 5% of the operating point in this study.

Second, the measured voltage and current of the VSC at PCC are calculated to obtain the impedance. The Park's transformation is used to transform the *abc*-frame signal to *dq*-frame. To achieve the impedance matrix, two independent perturbation signals are injected to gather enough information to solve the impedance matrix. The frequency-domain signal at the injected frequency are extracted with the FFT algorithm. The admittance of the VSC at a specific frequency is calculated as following [47],

$$\begin{bmatrix} Y_{dd} & Y_{dq} \\ Y_{qd} & Y_{qq} \end{bmatrix} = \begin{bmatrix} I_{d1} & I_{d2} \\ I_{q1} & I_{q2} \end{bmatrix} \begin{bmatrix} U_{d1} & U_{d2} \\ U_{q1} & U_{q2} \end{bmatrix}^{-1} \tag{3.1}$$

The operating point (V_d, V_q, I_d, I_q) and the frequency inputs are selected as the inputs of the impedance model.

Thus, the measurement and calculation are repeated with changing operating points. With the frequency scanning impedance measurement, the impedance dataset is established.

3.4. ANN MODEL GENERATION

To obtain the MOP-impedance, the ANN training technique is adopted. This part consists of two steps, the neural network initialization and the ANN training. In the neural network initialization step, the structure of the neural network is initialized with the domain knowledge VSC modeling. In the ANN training step, by feeding the measured data, the initialized neural network will be trained and the desired MOP-impedance model will be finally obtained.

3.4.1. MODEL INITIALIZATION

Different types of neural network are reported in previous literature [48]. In impedance identification, generating the impedance model with the measured data is a regression task, and the relationship of ANN is static. Thus, the feedforward neural network is suitable for this task.

The number of hidden layers and number of neurons is decided next. As reported in [49], one hidden layer has the capability to approximate every continuous function. Due to the physics of the impedance model, one hidden layer is enough for the impedance identification. However, there is no mathematical solution to decide the numbers of neurons of each hidden layer until now, so that the neurons number is optimized by trial-and-error.
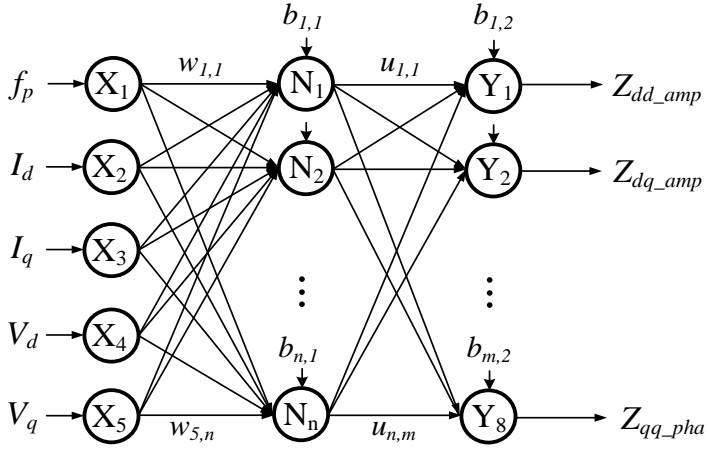
Figure 3-2. Diagram of ANN structure.

Therefore, a three-layer feedforward neural network model is initialized which is shown in Figure 3-2. Each neuron is a calculating unit with the weights $w_{i,j}$ ($i = 1,\ldots,$n, $j = 1,\ldots,$m) of each input and the bias b_j ($j = 1,\ldots,$m) of the output. The sigmoid function is selected as the activation function in the hidden layer, which is a nonlinear function [50]. Therefore, the calculation of each neuron in hidden layers can be represented as

$$y_j = S(\sum_{i=1}^{n}\left[w_{i,j} \cdot x_i + b_j \right]), j = 1,...,m \tag{3.2}$$

3.4.2. ANN TRAINING

In model training process, the MOP-impedance model is trained with the measured impedance data.

The ANN model is trained by feeding the measured dataset into the initialized neural network. The back-propagation is adopted to train the ANN while the typical mean squared error is used as the loss function, which is given by

$$MSE = \frac{1}{N}\sum_{n=1}^{N}\sum_{d=1}^{D}\left(\hat{X}_n^d \left(\boldsymbol{w}^l, \boldsymbol{b}^l \right) - X_n^d \right)^2 \tag{3.3}$$

where $\hat{X}_n^d \left(\boldsymbol{w}^l, \boldsymbol{b}^l \right)$ and X_n^d are the d-th calculated neurons and the training data index respectively; $\left(\boldsymbol{w}^l, \boldsymbol{b}^l \right)$ are the weights and bias to be trained.

After the model is generated, the coefficient of determination (R^2) is used to evaluate the performance of training [51-52], which is presented as

$$R^2 = 1 - \sum_i (y_i - f_i)^2 / \sum_i (y_i - \bar{y})^2 \qquad (3.4)$$

where y_i represents the output of training data and $\bar{y}$ is the average of y_i. f_i is the output of the trained model. In this case, the accepted R^2 is larger than 0.98.

After the ANN training step, the MOP-impedance model is generated.

3.5. CASE STUDY

To validate the proposed method, a case study with a grid-connected VSC control is designed, which is shown in Figure 3-3. The detailed parameters are shown in *Table 2-1*. The *d*-axis current is varying in the case study to make the result visible.
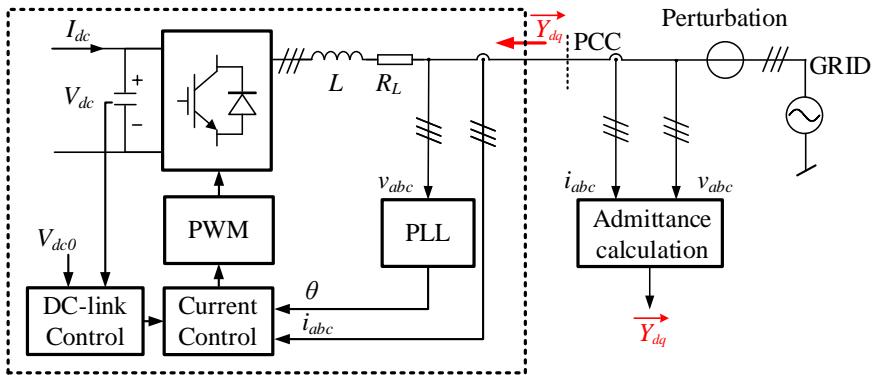
Figure 3-3. Admittance measurement diagram.

As shown in Figure 3-3, the voltage disturbance is injected into the VSC system to excite the output admittance data of VSC. In this case, the f_p is from 1 to 100 Hz with 1 Hz interval, and the *d*-axis current I_d is swept from 2.16 A to 9.84 A with 0.16 A interval. The outputs are separated into four elements, i.e., Y_{dd}, Y_{dq}, Y_{qd}, Y_{qq}. The measured admittance dataset is shown in Figure 3-4.

Symbol	Description	Value
V_{dc0}	Inverter dc voltage	730 V
V_{d0}	D-axis VSC voltage	250V
V_{q0}	Q-axis VSC voltage	0 V
I_{q0}	Q-axis VSC current	0 A
f_{sw}	Switching frequency	10 kHz
f_w	VSC frequency	50 Hz
L_f	Inverter inductor	3 mH
C_{dc}	Capacitor of dc-link	1000 µF
K_{p_dc}	dc voltage controller parameter	0.1
K_{i_dc}	dc-link controller parameter	10
K_{p_i}	current controller parameter	7.85
K_{i_i}	current controller parameter	2741.5
K_{p_pll}	PLL parameter	0.56
K_{i_pll}	PLL parameter	80.75

Table 3-1 VSC Parameters.
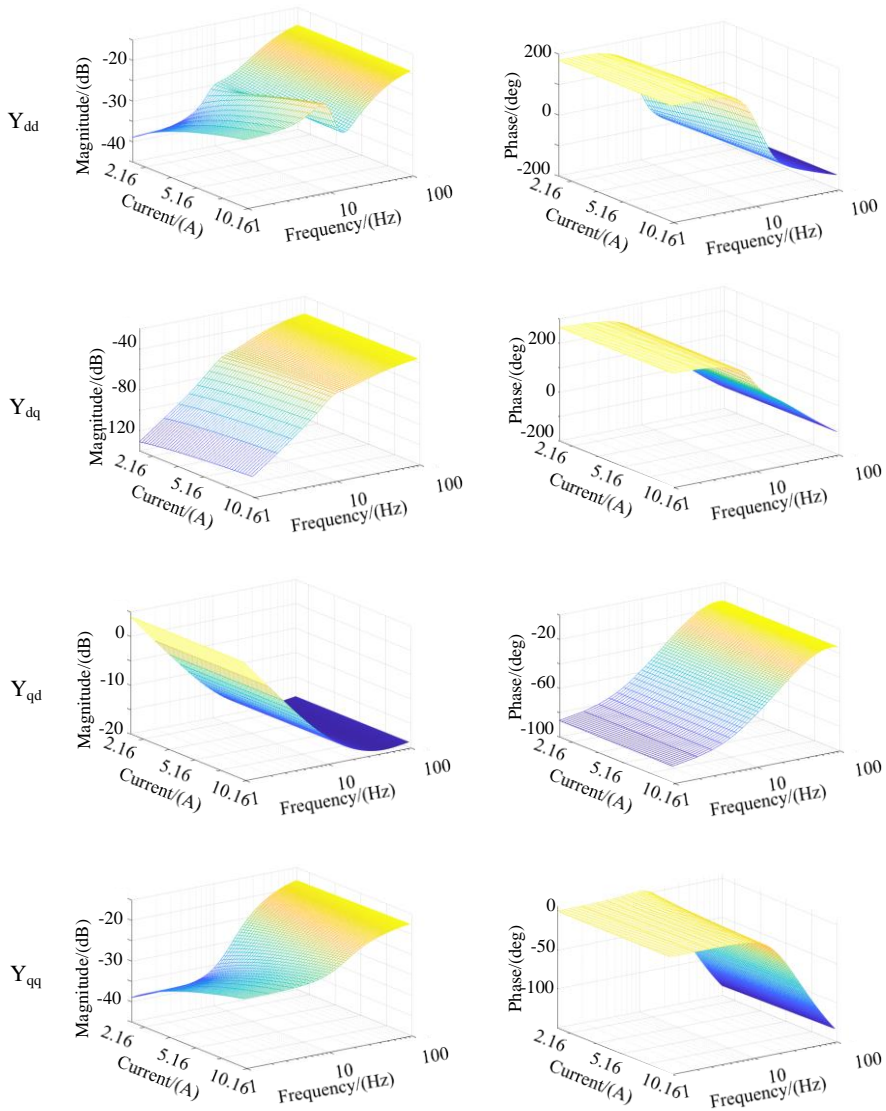
Figure 3-4. Measured admittance dataset of VSC.

The ANN model is trained by feeding the measured dataset, and then the MOP-admittance model Y_{ANN} is obtained as shown in Figure 3-5.
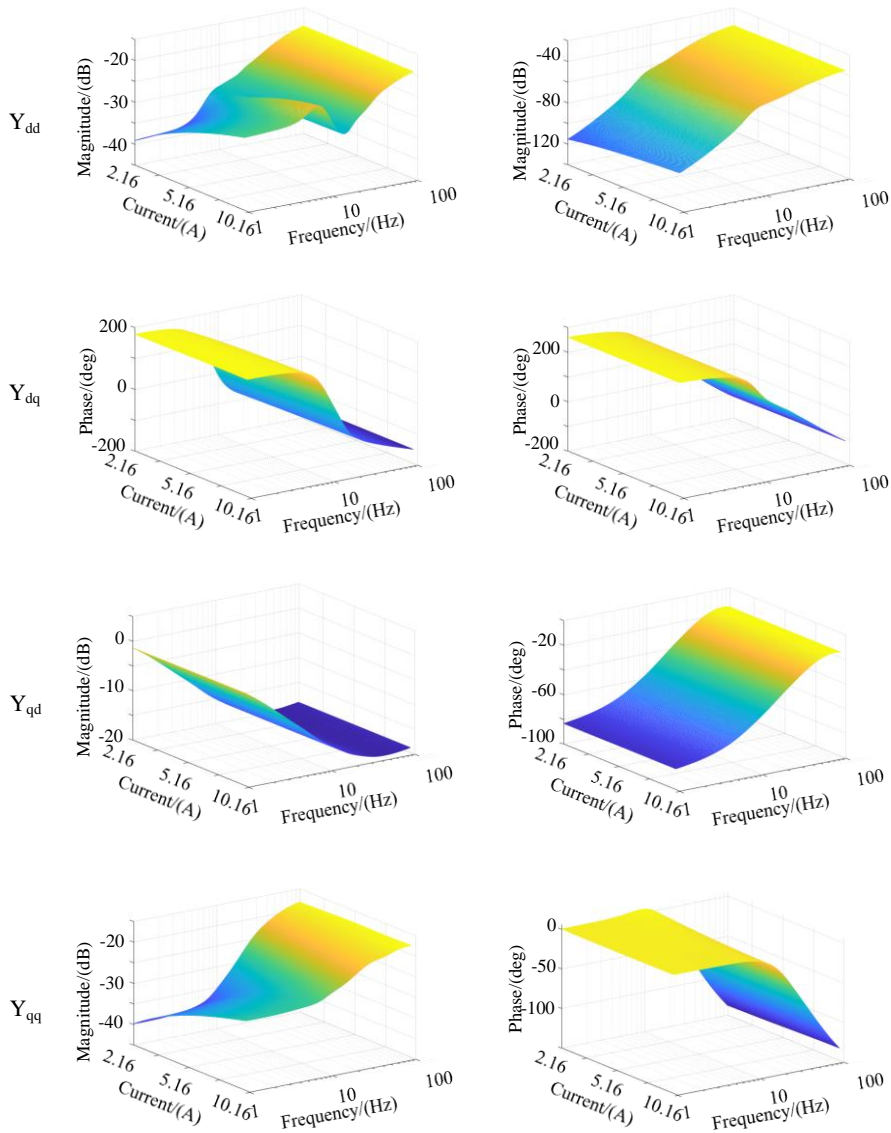
Figure 3-5. Generated MOP-admittance model.

To validate the generated MOP-admittance model, the model is compared with the field test data with the different frequency f_{p_v} and *d*-axis current I_{d_v}, where the f_{p_v} is from 1 to 100 Hz with 0.1 Hz interval and the *d*-axis operating current I_{d_v} is from 2.16 A to 9.84 A with 0.04 A interval.
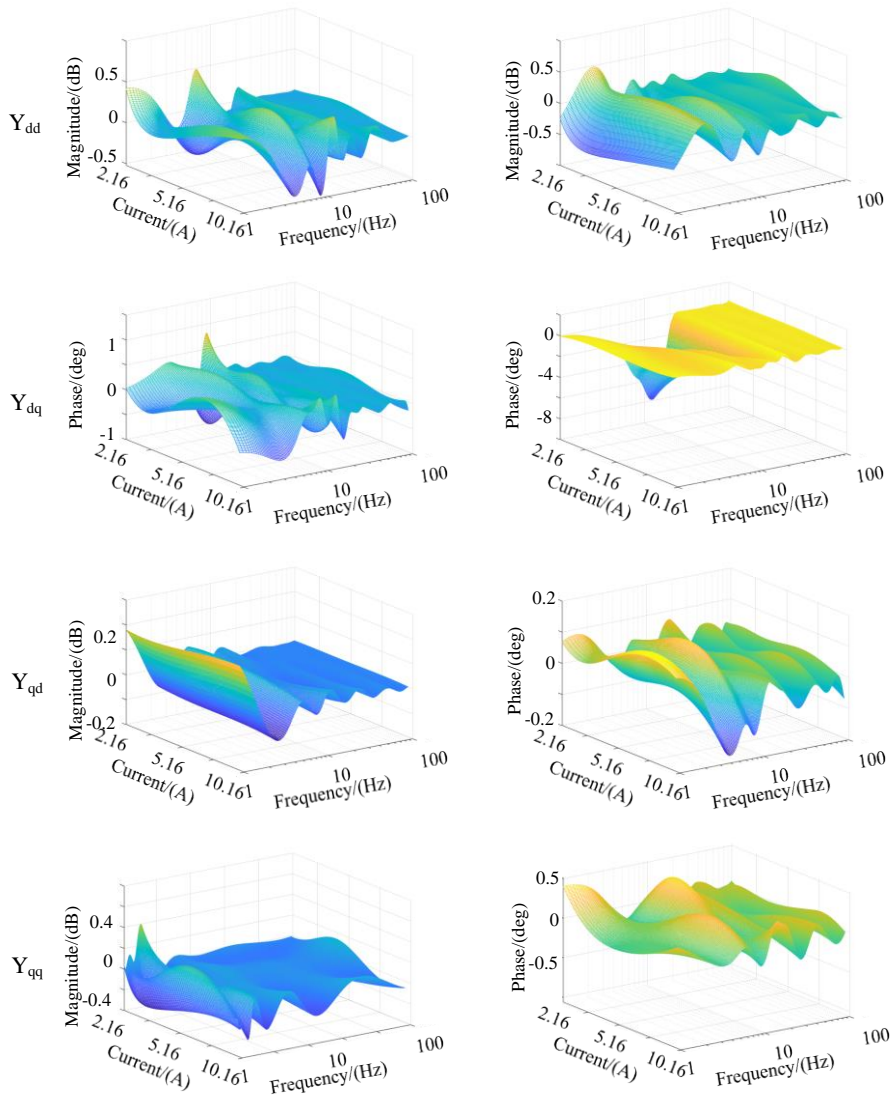
Figure 3-6. Errors of the generated MOP-admittance model.

Figure 3-6 shows the errors of the trained admittance model, where the biggest error is only less than 1 %. The comparison shows that the proposed method is effective in MOP-impedance modeling of the VSC.

3.6. **SUMMARY**

This chapter discusses ANN-based impedance identification for VSC. An ANN is
applied to model the VSC impedance considering the operating point changing. The
trained model could predict impedance of the VSC at the operating points that are not
measured. The case study validate the proposed method.

CHAPTER 4. TRANSFER LEARNING BASED MODELING OF VSC

The chapter is based on **J2, C2**.

4.1. BACKGROUND

Section 3 applies the artificial neural network (ANN) technique to identify the impedance model of the VSC. The ANN based MOP-impedance model is trained with the measured impedance, which can predict the accurate impedance of the VSC at varying operating points. Nevertheless, the data used in the model training is obtained through offline measurements. Since it is unrealistic to measure enough data through the online impedance identification, as the limited measured data amount will consequently introduce the over-fitting phenomena to the trained impedance model, and then affect the accuracy of stability analysis.

To overcome the bottleneck in online impedance identification, an online impedance identification method is proposed. The basic idea is to use the physical knowledge of VSC to facilitate the black-box modeling. Following this concept, we propose a new online impedance identification method that if a network can be constructed using the physical knowledge of VSC, the training effectiveness will be improved even with a small amount of data. Meanwhile, to improve the efficiency of online impedance identification, the transfer learning technique is integrated into the method by transferring offline knowledge to online impedance identification [53]. The proposed method consists of the following steps: First, the ANN model is constructed based on the derived analytical impedance model of the general VSC. Next, numerical offline tests are conducted to generate enough impedance data, which are fed into the constructed ANN structure to generate the offline impedance model. Then, based on transfer learning theory, the offline impedance model is transferred to online impedance identification of different VSCs by minimizing the distribution differences between the trained data and limited online field measured data iteratively. At last, the online impedance model is generated.

The chapter is organized as follows: The analytical impedance model of VSC is derived in Section 4.2. The framework of the proposed online impedance identification of VSC is stated in Section 4.3. In Section 4.4, the implementation of the proposed method is further explained. Finally, comparative case studies are provided in Section 4.5 that validate the proposed method.

4.2. GRID-CONNECTED VSC SYSTEM MODELING

Figure 4-1 shows the typical structure of grid-connected VSC controlled by the proportional integral (PI) current control loop and synchronous reference frame (SRF) PLL, where L and R_L are the inductor and the parasitic resistor, V_o and V_{pcc} are the output voltage and PCC voltage, I represent the inverter output current.
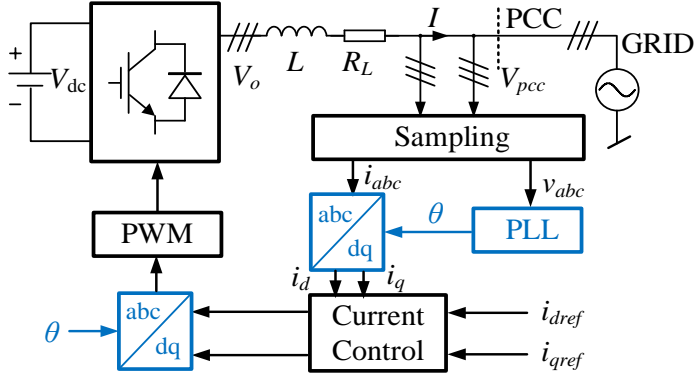
Figure 4-1. Diagram of grid-connected VSC system.
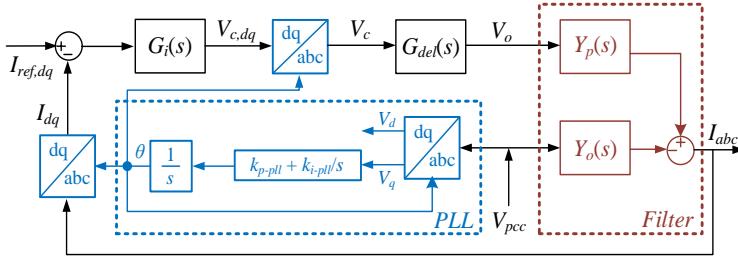
Figure 4-2. Control diagram of the grid-connected VSC.

Figure 4-2 shows the detailed control diagram of the grid-connected VSC. The filter plant is shown as follows:

$$Y_p(s) = Y_o(s) = \frac{1}{L \cdot s + R_L} \tag{4.1}$$

$G_i(s)$ is transfer function of the PI current controller, where k_p and k_i are the control parameters, which is written as:

$$G_i(s) = k_p + \frac{k_i}{s} \tag{4.2}$$

$G_{del}(s)$ is the time delay caused by the digital system [54], which consists of the computational delay (T_s) and pulse width modulator (PWM) delay ($0.5T_s$), where T_s is the sampling period. The time delay is shown below:

$$G_{del}(s) = e^{-1.5T_s \cdot s} \tag{4.3}$$

The PLL is linearized as follows [55]

$$\Delta\theta = G_{PLL}(s)\Delta V_q \tag{4.4}$$

$$G_{PLL}(s) = \frac{s \cdot k_{p-pll} + k_{i-pll}}{s^2 + (s \cdot k_{p-pll} + k_{i-pll})V_d} \tag{4.5}$$

where $k_{p\text{-}pll}$ and $k_{i\text{-}pll}$ are the control parameters of PLL, respectively. The dq-transformations used in the current control are linearized as follows:

$$I_{dq} = I\cos\theta + i \cdot I\sin\theta = (I + \Delta I)\cos(\Delta\theta + \theta) + i \cdot (I + \Delta I)\sin(\Delta\theta + \theta)$$
$$\rightarrow \Delta I_{PLL,dq} = i \cdot \Delta\theta \cdot I_{s,dq} \tag{4.6}$$

$$V_{dq} = V\cos\theta + i \cdot V\sin\theta = (V + \Delta V)\cos(\Delta\theta + \theta) - i \cdot (V + \Delta V)\sin(\Delta\theta + \theta)$$
$$\rightarrow \Delta V_{PLL,dq} = i \cdot \Delta\theta \cdot V_{s,dq} \tag{4.7}$$

where $I_{s,dq}$ and $V_{s,dq}$ denote the steady-state complex space vectors respectively, $\Delta I_{PLL,dq}$ and $\Delta V_{PLL,dq}$ are the dynamics of the PLL, respectively. Substituting (4.4) into (4.6) and (4.7),

$$\Delta I_{PLL,dq} = i \cdot G_{PLL}(s)\Delta V_q \cdot I_{s,dq}$$
$$\Delta V_{PLL,dq} = i \cdot G_{PLL}(s)\Delta V_q \cdot V_{s,dq} \tag{4.8}$$

The transfer functions with the superscript "m" represent the symmetric transfer matrices, which are shown below:

$$Y_{p,dq}^m(s) = Y_{o,dq}^m(s) = \frac{1}{L(s^2 + \omega_1^2)}\begin{bmatrix} s & \omega_1 \\ \omega_1 & s \end{bmatrix} \tag{4.9}$$

$$G_{i,dq}^m(s) = \begin{bmatrix} G_i(s) & 0 \\ 0 & G_i(s) \end{bmatrix} \tag{4.10}$$

$$G_{del}^m(s) = \begin{bmatrix} G_{del}(s) & 0 \\ 0 & G_{del}(s) \end{bmatrix} \tag{4.11}$$

where ω_1 is the fundamental frequency. The PLL dynamics is modeled as follows

$$\begin{bmatrix} \Delta I_{PLL,d} \\ \Delta I_{PLL,q} \end{bmatrix} = \begin{bmatrix} 0 & -G_{PLL}(s)I_{s,q} \\ 0 & G_{PLL}(s)I_{s,d} \end{bmatrix} \begin{bmatrix} \Delta V_d \\ \Delta V_q \end{bmatrix} = G_{I,PLL}^m \begin{bmatrix} \Delta V_d \\ \Delta V_q \end{bmatrix}$$

$$\begin{bmatrix} \Delta V_{PLL,d} \\ \Delta V_{PLL,q} \end{bmatrix} = \begin{bmatrix} 0 & -G_{PLL}(s)V_{s,q} \\ 0 & G_{PLL}(s)V_{s,d} \end{bmatrix} \begin{bmatrix} \Delta V_d \\ \Delta V_q \end{bmatrix} = G_{V,PLL}^m \begin{bmatrix} \Delta V_d \\ \Delta V_q \end{bmatrix} \tag{4.12}$$

where $I_{s,d}$, $I_{s,q}$ and $V_{s.d}$, $V_{s,q}$ denote the steady-state complex space vectors of current and voltage in d-axis and q-axis, respectively. Thus the block diagram of small-signal transfer matrices of the VSC system is derived as shown in Figure 4-3.
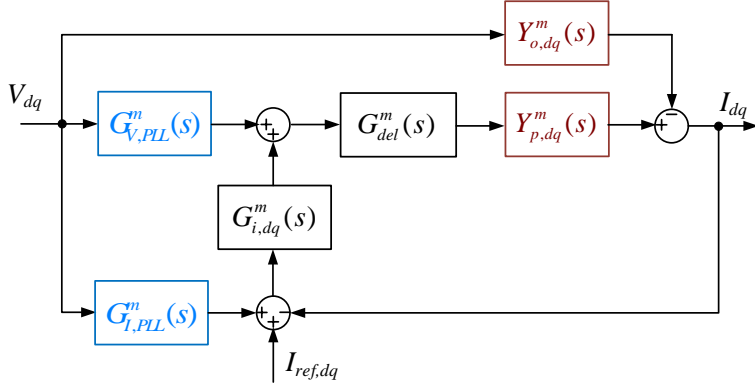
Figure 4-3. Small-signal transfer matrices diagram of the grid-connected VSC.

The transfer function is derived as:

$$\begin{bmatrix} I_d \\ I_q \end{bmatrix} = G_{cl,dq}^m(s) \begin{bmatrix} I_{ref,d} \\ I_{ref,q} \end{bmatrix}$$

$$- \left\{ \left[I^m + T_{dq}^m(s) \right]^{-1} Y_{to,dq}^m(s) - G_{cl,dq}^m(s) Y_{PLL}^m(s) \right\} \begin{bmatrix} V_d \\ V_q \end{bmatrix} \tag{4.13}$$

where I_m is the unitary diagonal matrix, the other transfer functions are shown below:

$$Y_{to,dq}^{m}(s) = Y_{p,dq}^{m}(s) - Y_{p,dq}^{m}(s)G_{del}^{m}(s)G_{V,PLL}^{m}(s)$$

$$T_{dq}^{m}(s) = Y_{p,dq}^{m}(s)G_{del}^{m}(s)G_{c,dq}^{m}(s) \qquad (4.14)$$

$$G_{cl,dq}^{m}(s) = \left[I^{m} + T_{dq}^{m}(s)\right]^{-1}T_{dq}^{m}(s)$$

Thus, the admittance matrix of VSC is derived as:

$$Y_{tcl,dq}^{m}(s) = \left[I^{m} + T_{dq}^{m}(s)\right]^{-1}Y_{to,dq}^{m}(s) - G_{cl,dq}^{m}(s)Y_{PLL}^{m}(s) \qquad (4.15)$$

As shown in (4.15), if the control structure of the VSC is fixed, the converter admittance model is dependent on the steady state operating point, frequency and the control parameters.

4.3. PROPOSED IMPEDANCE IDENTIFICATION

The black-box impedance of VSCs is the key to facilitate the study of converter-grid interaction stability. Actually, in real industrial practice, the circuit and control structures of VSCs provided by different vendors are usually known while the detail parameters cannot be accessed. Therefore, the idea of the proposed method is to utilize partial physics of the VSC and a small amount of online measured data to obtain the accurate model. The preliminary impedance model is generated at the offline phase to reduce the online training load, before the online identification.

The framework of the proposed physics informed neural network based online impedance identification is shown in Figure 4-4. As mentioned above, the implementation of the method is divided into the offline and online phase.

In the offline phase, the structure model of VSC that is first derived with the partial physics of the VSC is used to restructure the ANN structure, which can reduce the complexity of the ANN model and thus reduce the demand for data and training effort. Second, with the simulation model established in Matlab/Simulink, the offline impedance data are obtained with different setups compared with the online identification. After that, the offline ANN-based MOP-impedance model is trained with the initialized ANN structure and the simulated impedance data.

In the online phase, the distribution of the fielded data should be the same as the offline data. With the transfer learning technique, the field measured impedance data of the VSC with the impedance measurement technique are fed into the offline-trained impedance model, where the parameters and the structure of the ANN remain from the offline phase. After the online training, the MOP-impedance model of the VSC is achieved.
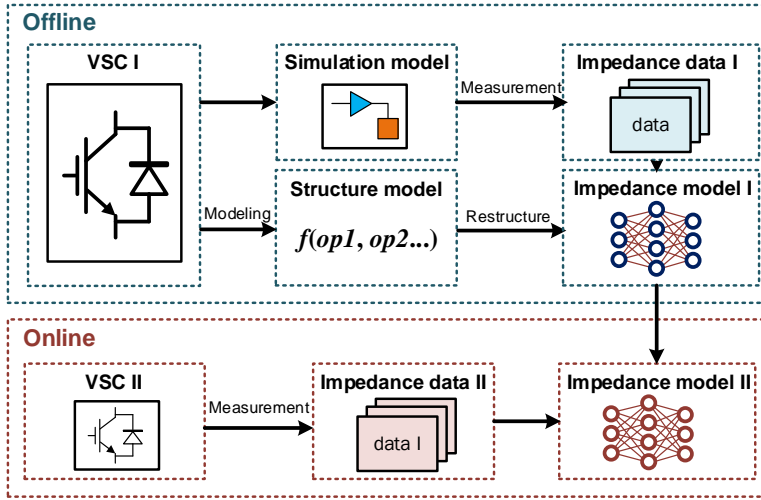
Figure 4-4. Framework of the proposed method.

4.4. IMPLEMENTATION OF PROPOSED METHOD

To implement the transfer learning based impedance identification method, *dq*-impedance measurement is proposed to obtain the data used for ANN training. And the ANN structure is generated with the analytical structure model derived in Section 4.2.

4.4.1. DQ-IMPEDANCE MEASUREMENT

The *dq*-impedance measurement is proposed in variable operating points and frequency to obtain the dataset.
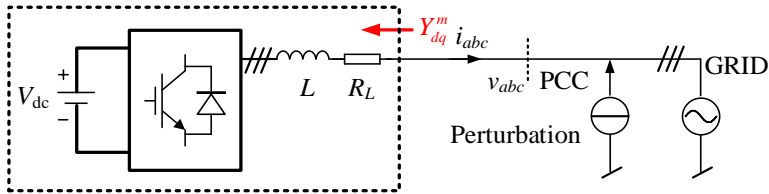
Figure 4-5. Dq-impedance measurement diagram.

Figure 4-5 shows the diagram of *dq*-impedance measurement of the VSC. Following the impedance measurement workflow in Section 3, the admittance of the VSC at the specific frequency f_p is calculated as follows.

$$Y_{dq}^m\left(f_p\right)=\begin{bmatrix} Y_{dd}\left(f_p\right) & Y_{dq}\left(f_p\right) \\ Y_{qd}\left(f_p\right) & Y_{qq}\left(f_p\right) \end{bmatrix}=\begin{bmatrix} U_{d1}\left(f_p\right) & U_{d2}\left(f_p\right) \\ U_{q1}\left(f_p\right) & U_{q2}\left(f_p\right) \end{bmatrix}^{-1}\begin{bmatrix} I_{d1}\left(f_p\right) & I_{d2}\left(f_p\right) \\ I_{q1}\left(f_p\right) & I_{q1}\left(f_p\right) \end{bmatrix} \quad (4.16)$$

Repeating the workflow by changing the frequency of the perturbation and operating point of VSC, the admittance dataset for training is established. The steady-state operating points of the VSC, i.e., V_d, V_q, I_d, I_q, are changing in different operating scenarios. Moreover, to reveal the characteristics of the VSC at the wide-band frequency, the frequency f_p is selected as the input of the model. Thus the structure of the MOP-impedance model is established, where the operating point of the VSC in dq-frame, i.e., (V_d, V_q, I_d, I_q) and frequency f_p are selected as the input of the model to reveal the operating-point-dependent and frequency-dependent feature.

4.4.2. ANN RESTRUCTURATION

The ANN training requires a large amount of data to configure the ANN structure and the weights of the connection. If some parts of the ANN can be pre-decided, the demand for data can be greatly reduced. Based on the derived theoretical admittance model of VSC, this section shows how to adopt this theoretical model to compress neural networks for the online impedance identification.

The admittance model in (4.16) can be transformed as follows:

$$Y_{dq}^m\left(s\right)=\left[A_{dq}^m(s)-B_{dq}^m(s)\cdot V_{dq}^m - C_{dq}^m(s)\cdot I_{dq}^m \right]\cdot\left[D_{dq}^m(s) \right]^{-1} \quad (4.17)$$

where:

$$O_{dq}^m(s) = \begin{bmatrix} \dfrac{s}{L \cdot (s^2 + \omega_1^2)} & \dfrac{\omega_1}{L \cdot (s^2 + \omega_1^2)} \\[3mm] -\dfrac{\omega_1}{L \cdot (s^2 + \omega_1^2)} & \dfrac{s}{L \cdot (s^2 + \omega_1^2)} \end{bmatrix}$$

$$P_{dq}^m(s) = \frac{s \cdot k_{pll-p} + k_{pll-i}}{s^2 + (s \cdot k_{pll-p} + k_{pll-i}) v_{1d}} \cdot k_p + \frac{k_i}{s} \cdot \begin{bmatrix} s & \omega_1 \\ -\omega_1 & s \end{bmatrix}$$

$$Q_{dq}^m(s) = \frac{1}{L(s^2 + \omega_1^2)} \cdot \frac{s \cdot k_{pll-p} + k_{pll-i}}{s^2 + (s \cdot k_{pll-p} + k_{pll-i}) v_{1d}} \cdot e^{-1.5T_s \cdot s} \cdot \left(k_p + \frac{k_i}{s} \right) \begin{bmatrix} s & \omega_1 \\ -\omega_1 & s \end{bmatrix}$$

$$R_{dq}^m(s) = \begin{bmatrix} 1 + \dfrac{1}{L(s^2 + \omega_1^2)} \cdot e^{-1.5T_s \cdot s} \cdot \left(k_p + \dfrac{k_i}{s} \right) \cdot s & \dfrac{1}{L(s^2 + \omega_1^2)} \cdot e^{-1.5T_s \cdot s} \cdot \left(k_p + \dfrac{k_i}{s} \right) \cdot \omega_1 \\[4mm] -\dfrac{1}{L(s^2 + \omega_1^2)} \cdot e^{-1.5T_s \cdot s} \cdot \left(k_p + \dfrac{k_i}{s} \right) \cdot \omega_1 & 1 + \dfrac{1}{L(s^2 + \omega_1^2)} \cdot e^{-1.5T_s \cdot s} \cdot \left(k_p + \dfrac{k_i}{s} \right) \cdot s \end{bmatrix}$$

$$V_{s,dq}^m = \begin{bmatrix} 0 & V_{s,d} \\ 0 & V_{s,q} \end{bmatrix}, I_{s,dq}^m = \begin{bmatrix} 0 & I_{s,d} \\ 0 & I_{s,q} \end{bmatrix}$$

$$(4.18)$$

As shown in (4.17)-(4.18), the admittance model is naturally separated into the operating point relevant function and the frequency relevant function. For simplification, (4.18) can be rewritten as:

$$O_{dq}^m(s) = \begin{bmatrix} O_{dd}(s) & O_{dq}(s) \\ O_{qd}(s) & O_{qq}(s) \end{bmatrix}, P_{dq}^m(s) = \begin{bmatrix} P_{dd}(s) & P_{dq}(s) \\ P_{qd}(s) & P_{qq}(s) \end{bmatrix},$$

$$Q_{dq}^m(s) = \begin{bmatrix} Q_{dd}(s) & Q_{dq}(s) \\ Q_{qd}(s) & Q_{qq}(s) \end{bmatrix}, \left[R_{dq}^m(s) \right]^{-1} = \begin{bmatrix} R_{dd}^{-1}(s) & R_{dq}^{-1}(s) \\ R_{qd}^{-1}(s) & R_{qq}^{-1}(s) \end{bmatrix}$$

$$(4.19)$$

Thus, (4.17) is derived as

$$Y_{dd}(s) = O_{dd}(s) R_{dd}^{-1}(s) + R_{qd}^{-1}(s) \cdot$$
$$\left(O_{qd}(s) - \left(V_q \cdot P_{dq}(s) + V_d \cdot P_{dd}(s) \right) - \left(I_q \cdot Q_{dq}(s) + I_d \cdot Q_{dd}(s) \right) \right)$$
$$Y_{qd}(s) = O_{qd}(s) R_{dd}^{-1}(s) + R_{qd}^{-1}(s) \cdot$$
$$\left(O_{qq}(s) - \left(V_d \cdot P_{qd}(s) + V_q \cdot P_{qq}(s) \right) - \left(I_d \cdot Q_{qd}(s) + I_q \cdot Q_{qq}(s) \right) \right)$$
$$Y_{dq}(s) = O_{dd}(s) R_{dq}^{-1}(s) + R_{qq}^{-1}(s) \cdot \tag{4.20}$$
$$\left(O_{qd}(s) - \left(V_q \cdot P_{dq}(s) + V_d \cdot P_{dd}(s) \right) - \left(I_q \cdot Q_{dq}(s) + I_d \cdot Q_{dd}(s) \right) \right)$$
$$Y_{qq}(s) = O_{qd}(s) R_{dq}^{-1}(s) + R_{qq}^{-1}(s) \cdot$$
$$\left(O_{qq}(s) - \left(V_d \cdot P_{qd}(s) + V_q \cdot P_{qq}(s) \right) - \left(I_d \cdot Q_{qd}(s) + I_q \cdot Q_{qq}(s) \right) \right)$$

Take Y_{dd} as example:

$$Y_{dd}(s) = F_1(s) - V_q \cdot F_2(s) - V_d \cdot F_3(s) - I_q \cdot F_4(s) - I_d \cdot F_5(s)$$
$$= G\left[V_q, V_d, I_q, I_d, F_1(s), F_2(s), F_3(s), F_4(s), F_5(s) \right] \tag{4.21}$$

The outputs of the neural network are written as follows:

$$Y_{dd-mag} = Mag\left[G\left[V_q, V_d, I_q, I_d, F_1(s), F_2(s), F_3(s), F_4(s), F_5(s) \right] \right]$$
$$Y_{dd-pha} = Ang\left[G\left[V_q, V_d, I_q, I_d, F_1(s), F_2(s), F_3(s), F_4(s), F_5(s) \right] \right] \tag{4.22}$$

where *Ang* and *Mag* are the nonlinear calculation function.

As a conclusion, based on the analytical impedance model of the VSC, the ANN is structured as shown in Figure 4-6. This structured neural network consists of 3 layers. Layer I is corresponding to the functions $F_1(s)$, $F_2(s)$, $F_3(s)$, $F_4(s)$, $F_5(s)$. Layer II is corresponding to function G. Layer III is corresponding to function *Mag* and *Ang*.
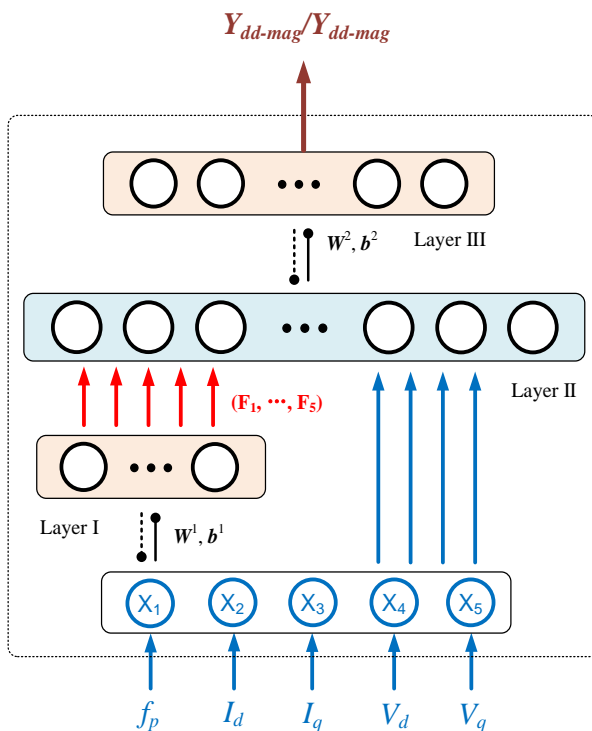
Figure 4-6. ANN structure diagram.

4.5. CASE STUDY

To validate the physics informed neural network, a case study of modeling the VSC systems is designed.

A target three-phase VSC system is marked as VSC II with the PI current controller and the PLL shown in Figure 4-1 is the target VSC. A known VSC is designed with the same control loop but different parameters and is marked as VSC I. The detailed parameters of the two VSCs are shown in Table I. In the case study setup, the VSC II is totally a black box while the VSC I is already known.

The task is to train the impedance model of VSC II using the known physics of VSC I and the limited online measured impedance of VSC II. Finally, the comparison between the conventional ANN based identification method and the proposed method using the same measured impedance dataset is conducted.

Symbol	Description	VSC I Value	VSC II Value
V_{dc}	DC voltage of VSC	700 V	700 V
f_0	Fundamental frequency	50 Hz	50 Hz
L_f	Inductor	1 mH	3 mH
R_{Lf}	Parasitic resistance of inverter inductor	0.3 mΩ	0.9 mΩ
K_{p_i}	Current controller parameters	10.5	31.4
K_{i_i}	Current controller parameters	5900	16449
K_{p_pll}	PLL parameters	1.2	1.4
K_{i_pll}	PLL parameters	257	324

Table 4-1. VSC parameters.

4.5.1. TRANSFER LEARNING BASED IMPEDANCE IDENTIFICATION

Before training the impedance model of the target VSC II, the impedance model of VSC I needs to be generated. To make the result easily visible, d-axis current I_d is changing. The frequency f_p is from 1 to 100 Hz with 1 Hz interval, and the d-axis current I_d is from 20 A to 70 A with 1 A interval. Figure 4-7 shows the measured dataset. The measured data are fed into the restructured ANN and the model is trained. At last, the admittance model of the source VSC Y_{VSC-I} is generated as shown in Figure 4-8.
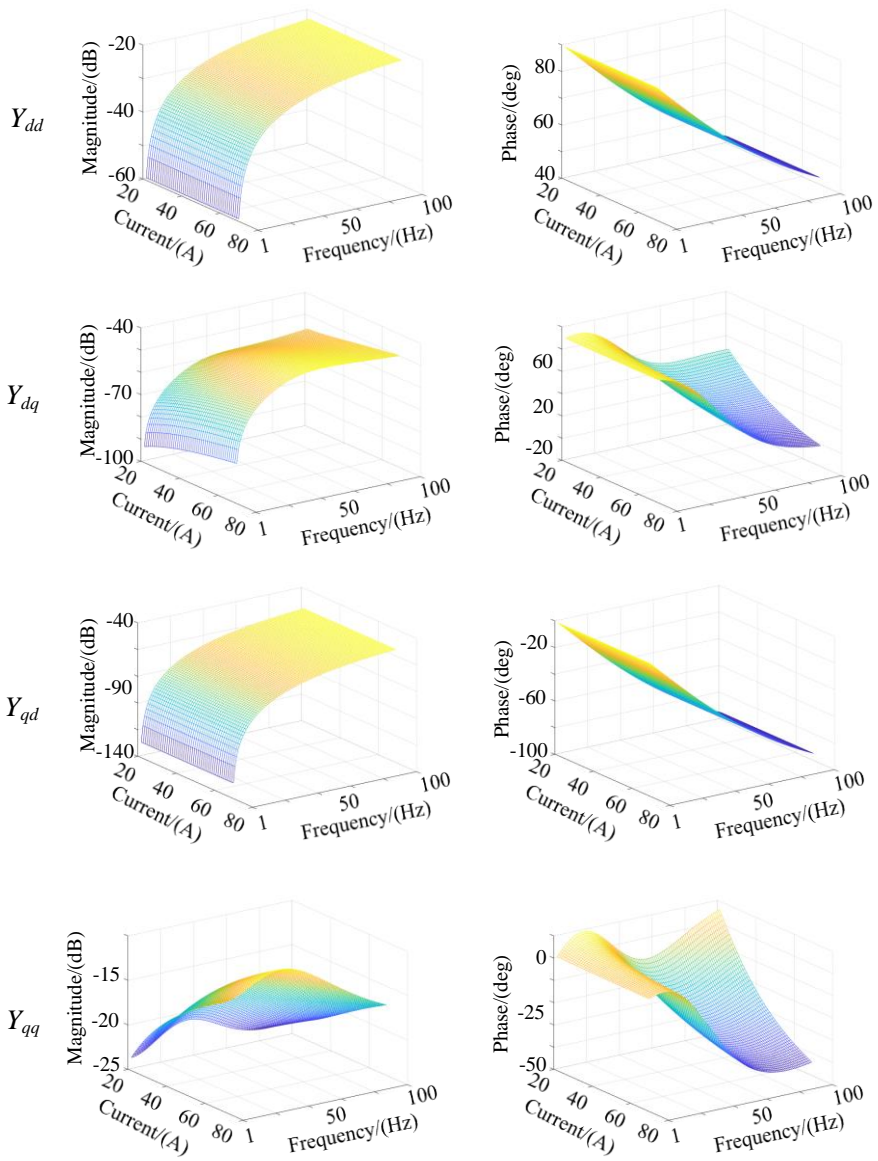
Figure 4-7. Measured admittance dataset of source VSC.
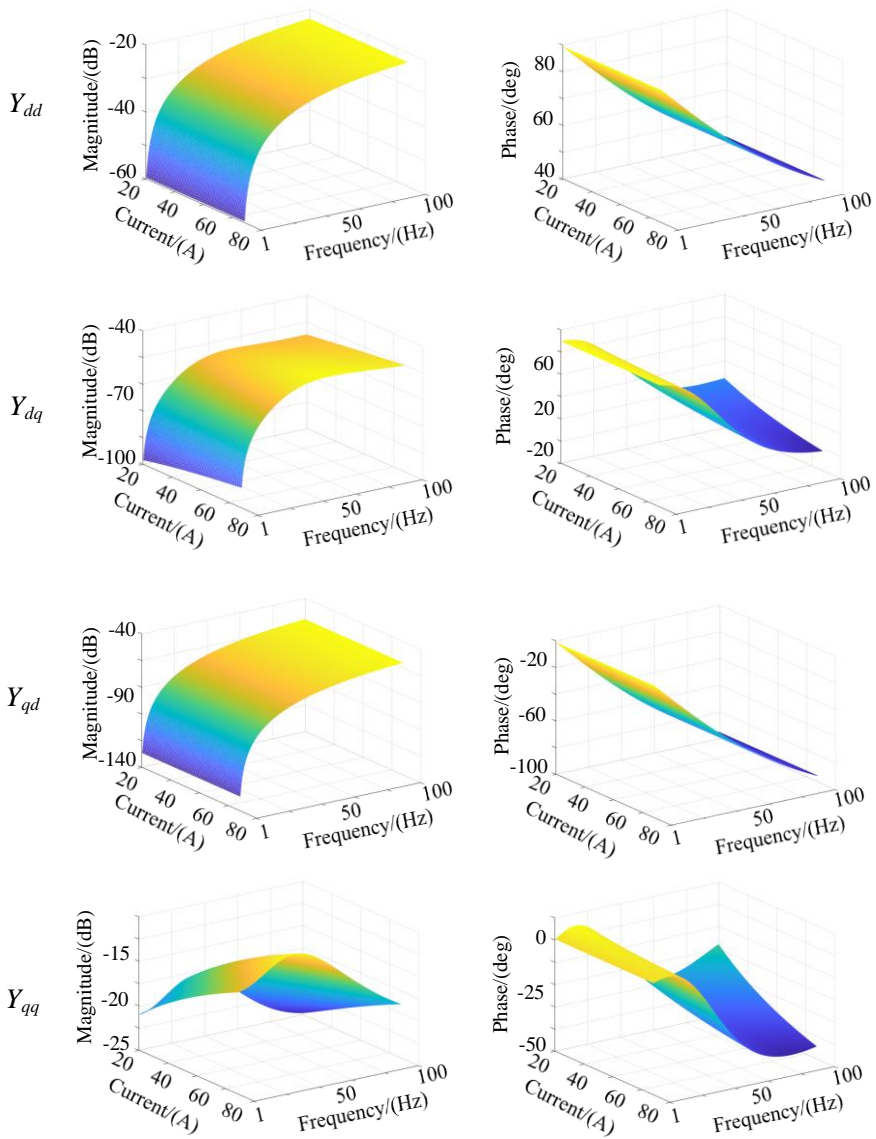
Figure 4-8. Generated MOP-admittance model of source VSC.
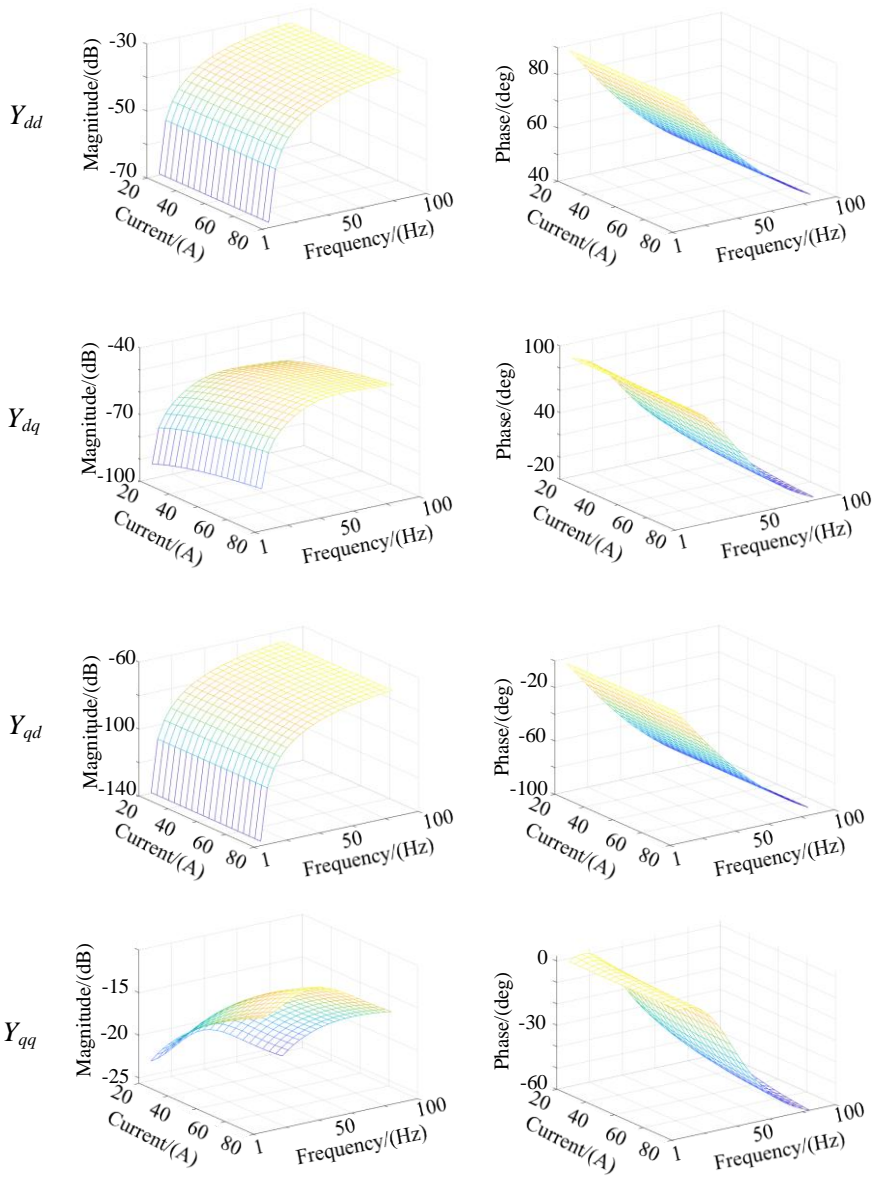
Figure 4-9. Measured admittance dataset of target VSC.
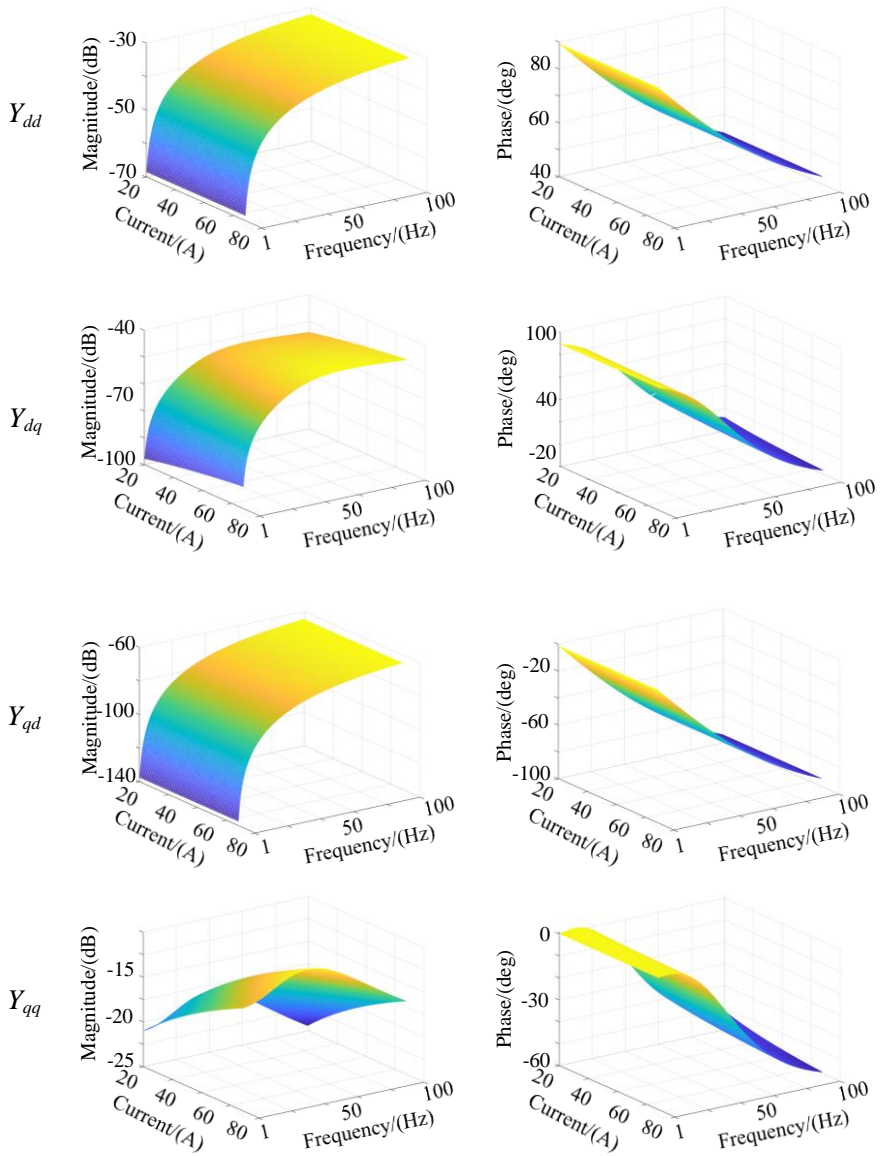
Figure 4-10. Generated MOP-admittance model of source VSC.
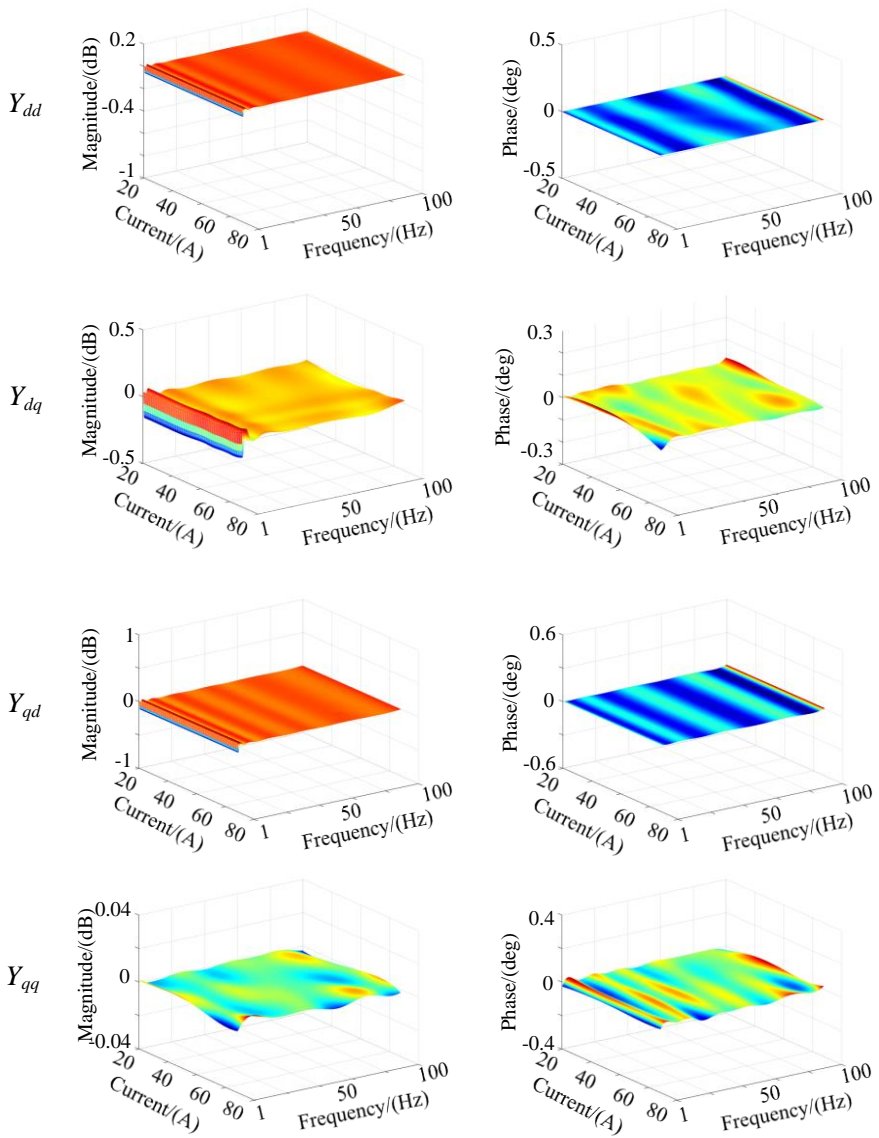
Figure 4-11. Errors between generated admittance model and measured data using proposed method.
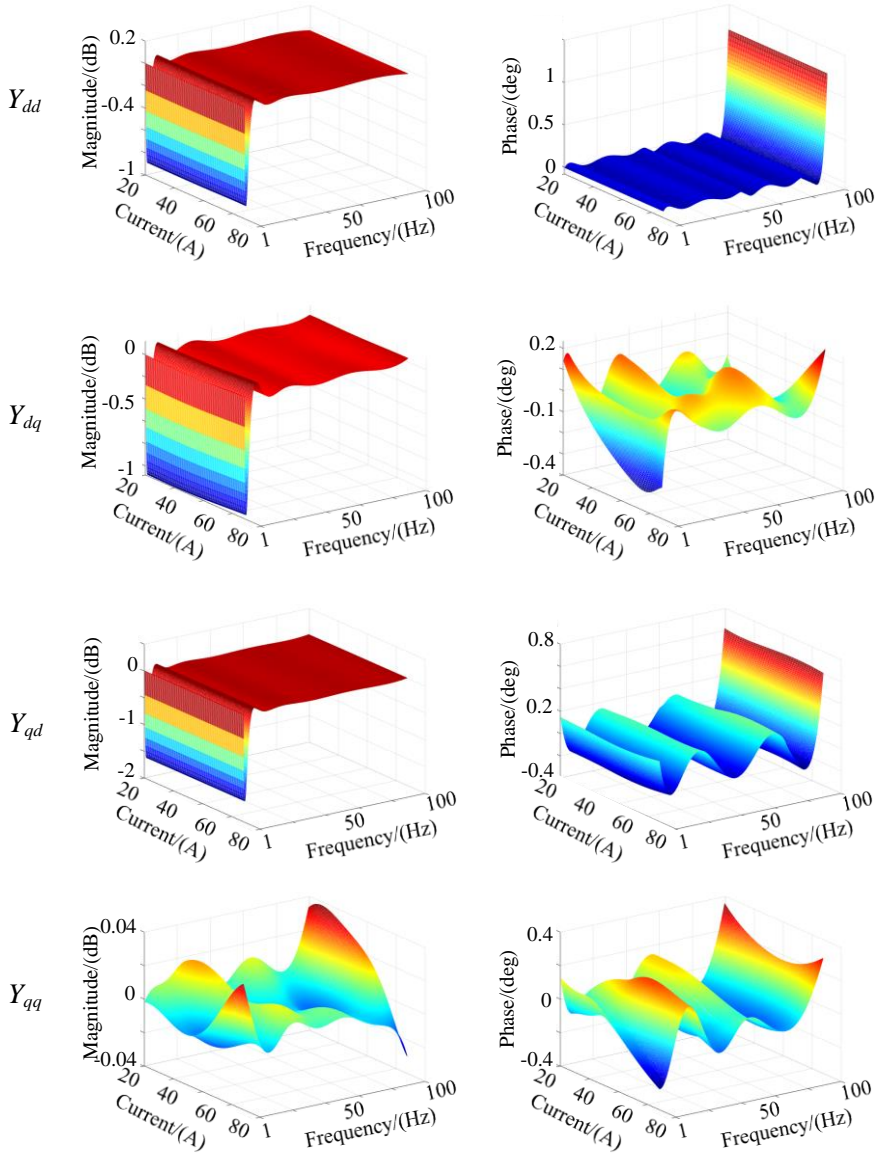
Figure 4-12. Errors between generated admittance model and measured data using conventional ANN method.

The source VSC model is used to train the admittance model of the target VSC. In the impedance dataset of target VSC, the frequency f_p is from 1 Hz to 101 Hz with 5 Hz interval, while the d-axis current I_d is from 20 A to 70 A with 5 A interval. In online measurement, only 200 data points are acquired, which are shown in Figure 4-9. Then

feed the dataset into the admittance model Y_{VSC-I}. The admittance model of the target VSC Y_{VSC-II} is generated, which is shown in Figure 4-10.

The trained admittance model Y_{VSC-II} is compared with the field measured data. In the field measured dataset, the corresponding frequency f_{p_v} is from 1 to 100 Hz with 0.1 Hz interval, while the corresponding d-axis current I_{d_v} is from 20 A to 70 A with 0.1 A interval. The corresponding errors are shown in Figure 4-11, where the error is less than 1 %. Hence, the comparison shows that the proposed method is effective in online impedance model identification of the VSC.

4.5.2. COMPARISON WITH THE CONVENTIONAL ANN METHOD

The conventional ANN method and the proposed method using the same measured impedance dataset. The same dataset as shown in Figure 4-10 is fed into a two-hidden-layer random initialized ANN. After the training, the model $Y_{VSC-II-O}$ is generated. To directly show the comparison result of two models. The corresponding errors between the verification data with the same distribution and the generated model are shown in Figure 4-12.

As shown in Figure 4-11, the conventional ANN method cannot have a good performance with the sparse dataset, while the proposed method can accurately establish the impedance model of VSC even with limited data amount.

4.6. SUMMARY

This chapter proposes a new impedance identification method using transfer learning for online impedance identification of VSC under changing operating points. Considering the data amount limitation in online impedance measurement, the physics informed neural network based impedance identification is developed in this paper. The partial physics of the VSC is used to compress the artificial neural network, which can reduce the calculation burden of online impedance identification. Meanwhile, the two-steps impedance identification is developed with the inspiration of the transfer learning theory to further increase the online impedance identification efficiency. The proposed method could be used for online impedance identification effectively.

CHAPTER 5. DNN BASED STABILITY ESTIMATION

The chapter is based on **J3**.

5.1. BACKGROUND

As the online impedance model is generated in Section 4. The generated ANN-based impedance model accurately predicts the impedance at a wide range of operating points, which could be used for point-wise stability analysis with the Nyquist stability criterion. However, the efficiency of this point-wise stability analysis is not promising considering the uncertain and intermittent operation of renewables, as the stability evaluation should be re-performed when the operating point changes. Moreover, it is hard to predict the stability margins in just a few estimations when the operating point has multiple dimensions [56].

This chapter attempts to fill this research gap by proposing a double-DNN based stability analysis framework considering the operating point variations. First, a DNN based MOP-impedance model is established by frequency scanning at various scenarios with different operating points. Second, a DNN based stability discriminant model is developed for the estimation of the stability region. The double DNN based stability analysis framework achieves fast and accurate estimation of the stability region for grid-converter interaction considering the variation of operating points.

The chapter is organized as follows. Section 5.2 introduces the proposed framework. Section 5.3 and Section 5.4 gives the practical implementation of the proposed method in impedance model generation and stability discrimination model generation respectively. The experimental test results are provided in Section 5.5, which validate the proposed method.

5.2. FRAMEWORK OF BLACK-BOX DNN-BASED STABILITY ANALYSIS OF GRID-CONVERTER SYSTEM
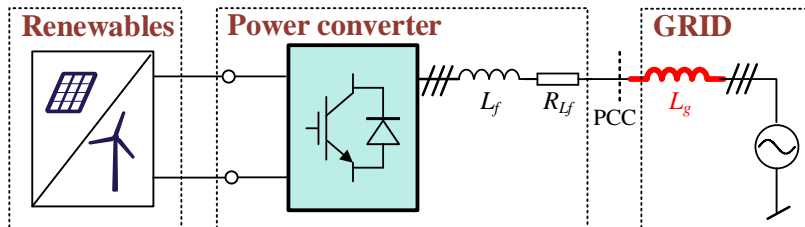
5.2.1. SYSTEM DESCRIPTION

Figure 5-1. Diagram of the renewables integrated grid-connected VSC system.

Figure 5-1 shows the relatively common topology of renewables integrated grid-connected VSC systems. The input of the VSC is connected with the renewables while the output is connected with the power grid through the filter L_f and its parasitic resistance R_{Lf} at the PCC. Grid impedance is denoted as L_g. In such a system, the inductor of VSC and power cables interact with the inner control loops of the VSC resulting in oscillations and instability. On the other hand, the uncertainties of the renewables and loads also bring the variation of operating points of the VSC, which affect stability analysis of the interaction system. Therefore, it is of high importance to develop a MOP-impedance model to study the interaction between VSC and grid, and analyze the stability of the system.

5.2.2. FRAMEWORK DESCRIPTION

Figure 5-2 shows the double DNN-based stability analysis framework, which consists of two implementation steps.

First is to develop the DNN-based MOP-impedance model. As the impedance model of VSC varies with the operating point. To deal with operating point variations, the operating point scanning measurement is carried out with various operating points. **op** denotes the operating point set, which is a vector consisting of different types of operating points (*op1*, *op2*…). And then the frequency scanning impedance measurement is implemented to acquire the impedance spectrum in the full frequency domain. With the data measured from the above procedure fed, the DNN is trained. After the training, a DNN based MOP-impedance model is trained.

The second step is to develop the DNN based stability discrimination model. Based on the DNN based MOP impedance model developed in the first step, as well as the grid impedance model and generalized Nyquist criterion, the stability data can be generated. Then the DNN based stability discrimination model can be constructed to

show the stability probability state of the renewables integrated grid-connected VSC system at variable operating points considering the uncertainties of renewables.

Finally, the stability region can be generated based on the discrimination model in the second step by inputting the concerned operating point range into the discrimination model.
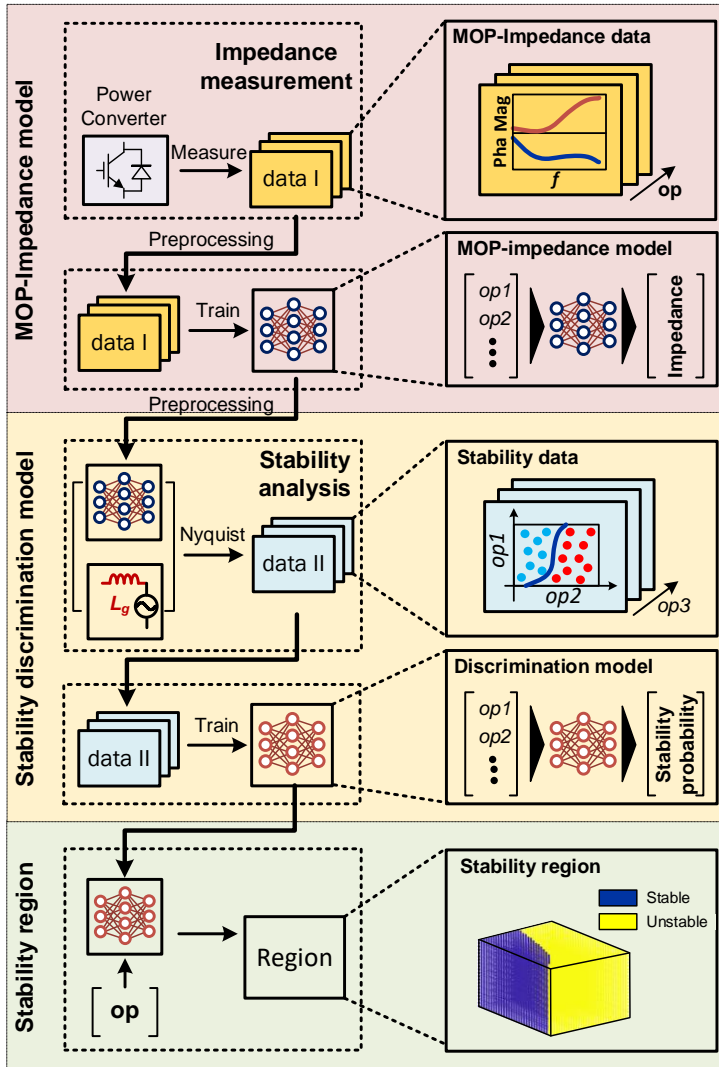
Figure 5-2. Proposed framework of the double DNN based stability analysis of grid-converter interaction system.

5.3. PROPOSED DNN BASED MOP-IMPEDANCE MODEL

The MOP-impedance model generation step employs the impedance measurement and DNN training techniques to generate the MOP-impedance model. The implementation consists of the MOP-impedance measurement and MOP-impedance model training.

5.3.1. MOP-IMPEDANCE MEASUREMENT

The MOP-impedance data is acquired by the frequency scanning in different operating points. **Error! Reference source not found.** shows the impedance measurement diagram.

Follow the workflow described in Section 3, the impedance of the VSC is calculated as following:

$$Z_{dq} = \begin{bmatrix} Z_{dd} & Z_{dq} \\ Z_{qd} & Z_{qq} \end{bmatrix} = \begin{bmatrix} V_{d1} & V_{d2} \\ V_{q1} & V_{q2} \end{bmatrix} \begin{bmatrix} I_{d1} & I_{d2} \\ I_{q1} & I_{q2} \end{bmatrix}^{-1} \tag{5.1}$$

where the Z_{dq} is the dq-frame VSC impedance.

5.3.2. MOP-IMPEDANCE MODEL TRAINING
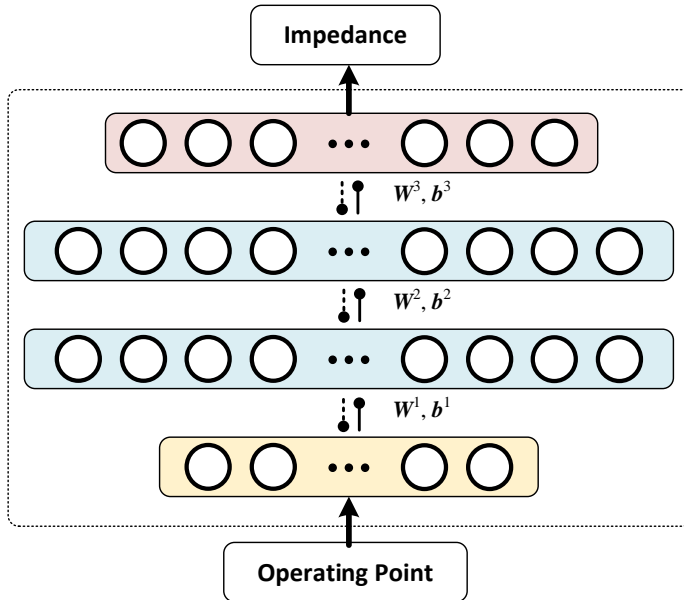
Figure 5-3. DNN structure of MOP-impedance model.

First, the DNN model is initialized based on the physical nature of the impedance. The architecture adopted in this paper is a feed-forward neural network to represent a highly non-linear function that maps the operating point of the VSC to its impedance model [57]. A feedforward DNN shown in Figure 5-3 contains four layersrs, which contain different numbers of neurons. The type of activation function in hidden neurons is sigmoid, while the output neurons are linear. The random initialization is suitable for impedance identification due to its high nonlinearity [58], [59].

The back-propagation is adopted to train the DNN model with the typical mean squared error loss function [60-61], which is given by

$$MSE = \frac{1}{N} \sum_{n=1}^{N} \sum_{d=1}^{D} \left(\hat{X}_n^d \left(\boldsymbol{w}^l, \boldsymbol{b}^l \right) - X_n^d \right)^2 \tag{5.2}$$

where $\hat{X}_n^d \left(\boldsymbol{w}^l, \boldsymbol{b}^l \right)$ and X_n^d are the d-th calculated neurons and the training data index respectively; $(\boldsymbol{w}^l, \boldsymbol{b}^l)$ are the weights and bias to be trained.

During the learning process, a DNN is used to learn the mapping of the relationship of impedance. It can automatically learn the complicated relationship to the impedance from the operating points given the sufficient training samples. This process needs to be executed several times and the impedance model is then generated.

5.4. DNN-BASED STABILITY DISCRIMINATION MODEL

A DNN-based stability discrimination model is proposed to generate the stability condition of the grid-connected VSC system under changing operating points. As the mapping from the operating points to the system stability condition is highly nonlinear, the stability discrimination model is developed based on the DNN technique with the developed MOP-impedance model in Section 5.3. The implementation consists of the stability condition data generation and stability discrimination model generation.

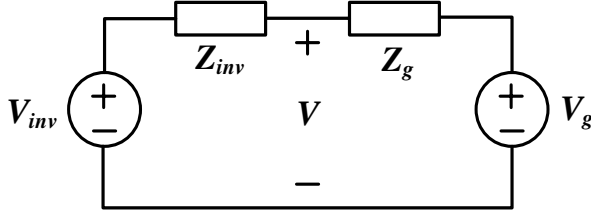## 5.4.1. STABILITY CONDITION DATA GENERATION

Figure 5-4. Equivalent circuit of interaction system.

The generalized Nyquist criterion is widely applied for the system stability assessment of the MIMO system. The grid-converter system shown in Figure 5-2 is modeled as two subsystems connected at the PCC. According to Thevenin's theorem, each subsystem is represented as the impedance in parallel with the voltage source which is shown in Figure 5-4where Z_{inv} is the VSC impedance, which is developed in Section III, while Z_g is the equivalent grid impedance. The impedance ratio is given below

$$Le(j\omega) = Z_g(j\omega) \cdot Z_{inv}^{-1}(j\omega) \tag{5.3}$$

The stability of grid-converter interaction system is predicted by the eigenlocus which are the locus of the eigenvalues of the impedance ratio parameterized as a function of frequency and is derived as

$$\det\left[\lambda I - Le(j\omega)\right] = 0 \tag{5.4}$$

If the impedance ratio $Le(s)$ has P unstable poles, then the grid-connected VSC system is stable only if the eigenlocus of the impedance ratio, take together, encircle the $(-1, j0)$ P times [62].

Based on the generalized Nyquist criterion theory, the stability condition at each operating point can be discriminated and the stability condition data are generated. The stability condition data consists of a feature space of operating points $\mathbf{X}$ and the corresponding class label y (stable or unstable), which are represented as $\{(\mathbf{x_1}, y_1), \ldots, (\mathbf{x_n}, y_n)\}$, where $\mathbf{x}$ contains four elements of the operating points (v_d, v_q, i_d, i_q).

5.4.2. DNN-BASED STABILITY DISCRIMINATION MODEL TRAINING

The stability discrimination model is developed based on DNN due to the high nonlinearity of the relationship.
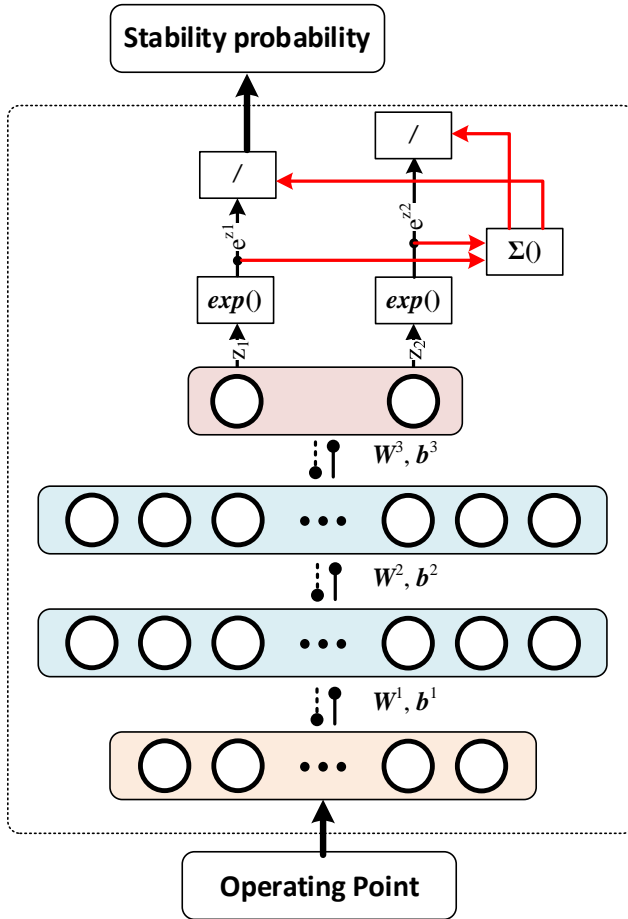
Figure 5-5. DNN structure of stability discrimination model.

The DNN adopted here is a feed-forward neural network with a logical regression layer and serves as the multi-layer perceptron. As shown in Figure 5-7, the structure of DNN-based stability discrimination mode contains four layers. The input of the model is the operating point while the output is the stability probability. The activation function in hidden layers is sigmoid, while the softmax function is embedded in the output layer to generate the probability of stability [63], which is given by:

$$p(z_1) = \frac{e^{z_1}}{e^{z_1} + e^{z_2}} \tag{5.5}$$

where $p(z_1)$ denotes the probability of the output z_1, here z_1 and z_2 are the output of the neural nodes in the output layer, which represent the stable state and unstable state of the system respectively.

The back-propagation with the logarithmic loss function is used to train the DNN model [64]. The binary entropy function is the evaluation of the performance of logical regression algorithms, which is given by:

$$LL = -\sum_{k} t_k \cdot \ln P_k \qquad (5.6)$$

where t_k denotes the label of the stable state in each reference sample, where t_k is equal to 1 when the system is stable, while P_k denotes the probability of t_k. After the training process, the DNN-based stability discrimination model that can be used for stability analysis of the grid-converter interaction is generated.

5.5. CASE STUDIES

To verify the proposed method in Figure 5-2 it is applied to a VSC system in which the VSC is controlled with the PR current controller and the phase-locked loop (PLL) shown in Figure 5-6, where the detailed VSC parameters are shown in Table 5-1. The VSC is synchronized to the power grid with the PLL. The power reference P_{ref} and Q_{ref} are varied with the renewables. The variation of grid voltage are also taken into consideration. In this chapter, the voltage and current in dq-axis are selected as the operating point, the relationship between these elements is shown below:

$$\begin{cases} P = I_q \cdot V_q + I_d \cdot V_d \\ Q = I_q \cdot V_d + I_d \cdot V_q \\ \theta = \arctan\left(\dfrac{V_q}{V_d}\right) \\ U = \dfrac{V_d}{\cos\theta} \end{cases} \qquad (5.7)$$

As shown in (5.7), the system operating point is dependent on the voltage and current. Due to the PLL effect, the voltage of the VSC in the q-axis is aligned to the voltage reference at PCC, i.e., $v_q = 0$. Thus, the system operating point can be represented as the vector (v_d, i_d, i_q).

Following the proposed framework in Figure 5-2, , the MOP-impedance model is first established with the operating-point-scanning impedance measurement technique and DNN training technique; then the established impedance model is used for the DNN-based stability discrimination model generation; at last, the stability region of the grid-connected VSC system is generated with the stability discrimination model.

5.5.1. MOP-IMPEDANCE MODEL

Symbol	Description	Value
V_{dc}	DC voltage	700 V
f_{sw}	Switching frequency	10 kHz
f_0	Fundamental frequency	50 Hz
L_f	Inverter inductor	3 mH
R_{Lf}	Parasitic resistance of inverter inductor	0.9 mΩ
L_g	Grid inductor	18 mH
K_{p_i}	Current controller parameters	2.8
K_{r_i}	Current controller parameters	1302
K_{p_pll}	PLL parameters	31.41
K_{i_pll}	PLL parameters	16449

Table 5-1. VSC Parameters.

Symbol	Range	Interval
f	1 Hz to 100 Hz	1 Hz
I_d	0 A to 20 A	1 A
I_q	-60 A to 60 A	20 A
V_d	300 V to 400 V	20 V

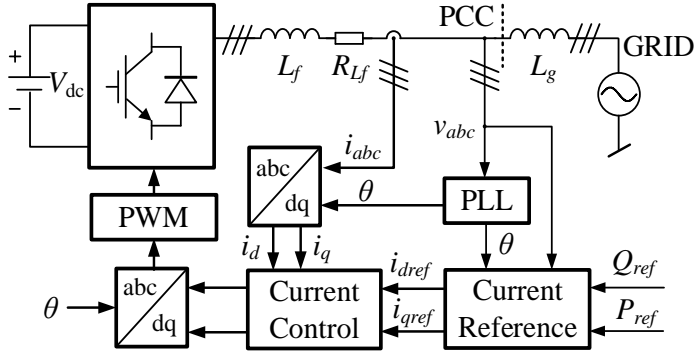*Table 5-2. Training Dataset Parameters.*

Figure 5-6. Grid-connected VSC diagram.

The current perturbation is injected into the grid-connected VSC as shown in Figure 5-6 and after the calculation, the dataset is established. The inputs of the dataset are the frequency and operating point, where frequency f_p and the operating points I_d, I_q, V_d are swept with the different ranges and intervals separately as shown in Table 5-2, the outputs are the impedance of the VSC. The dataset structure is shown in Figure 5-7. To make the results easily visible, only the variation of I_d is drawn in this thesis. The obtained dataset is shown in Figure 5-8. Then the training dataset is fed into the DNN as shown in Figure 5-3. After the training, the MOP-impedance model Y_{ANN} is generated as shown in Figure 5-9.
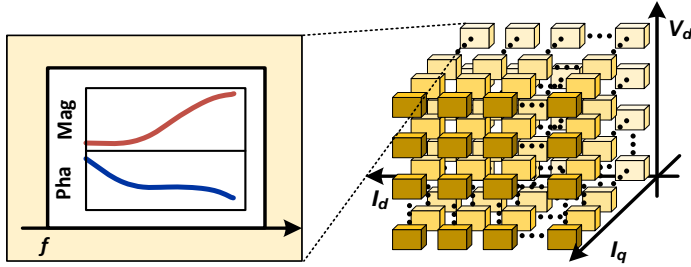
Figure 5-7. Dataset structure.

The accuracy of the MOP-impedance model is evaluated by the index R^2, which is given by

$$R^2 = 1 - \sum_i \left(y_i(X_i) - f_i(X_i) \right)^2 / \sum_i \left(y_i(X_i) - \overline{y} \right)^2 \tag{5.8}$$

where X_i denotes the operating point and frequency, y_i denotes the reference impedance data corresponding to the X_i in the verification dataset, $\overline{y}$ denotes the

average value, f_i denotes the trained DNN model. In this thesis, the threshold of R^2 is set to 0.99.

Figure 5-8. Output impedance dataset of VSC.

Figure 5-9. Generated MOP- impedance model of VSC.

5.5.2. DNN-BASED STABILITY DISCRIMINATION MODEL

The grid impedance is a three-phase inductor, which is shown as

$$Z_{gabc} = \begin{bmatrix} j2\pi f \cdot L_g & 0 & 0 \\ 0 & j2\pi f \cdot L_g & 0 \\ 0 & 0 & j2\pi f \cdot L_g \end{bmatrix} \tag{5.9}$$

where f is the sweeping frequency. Then in dq-frame the grid impedance is written as follow

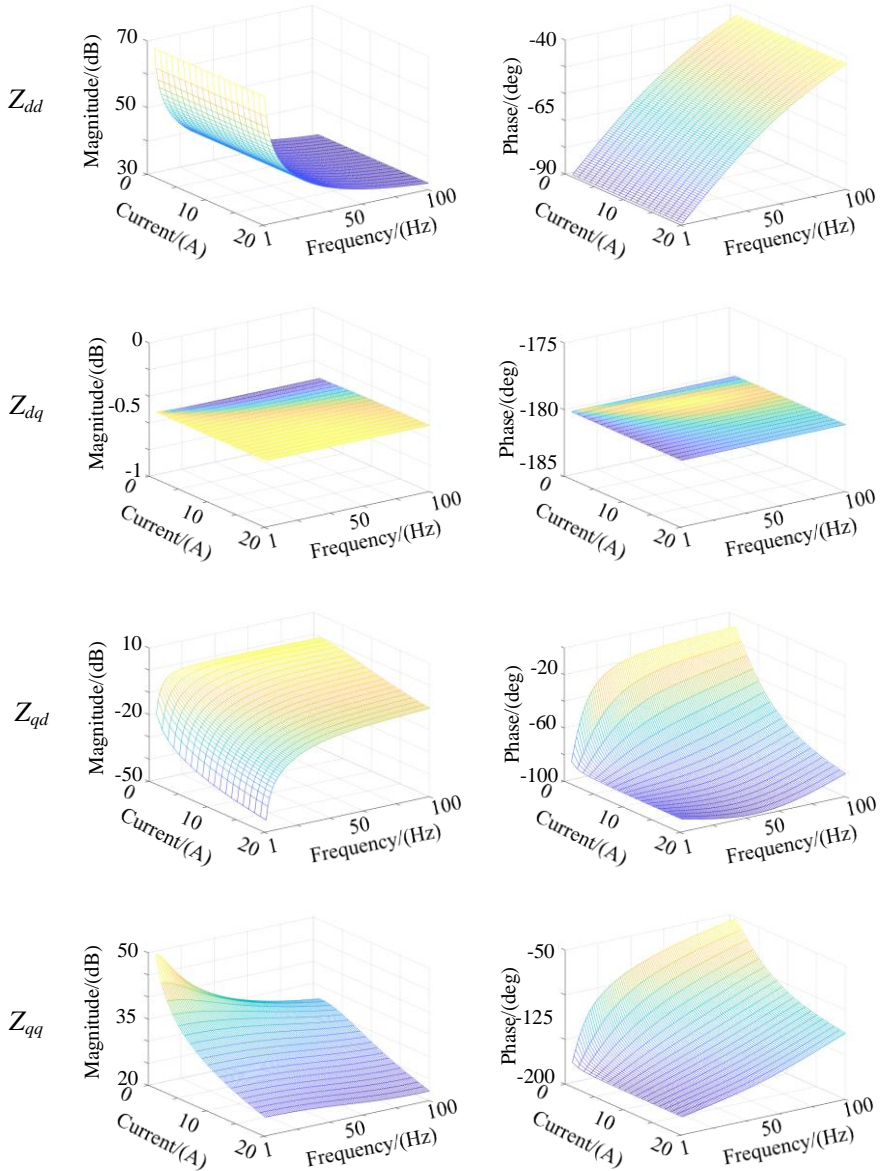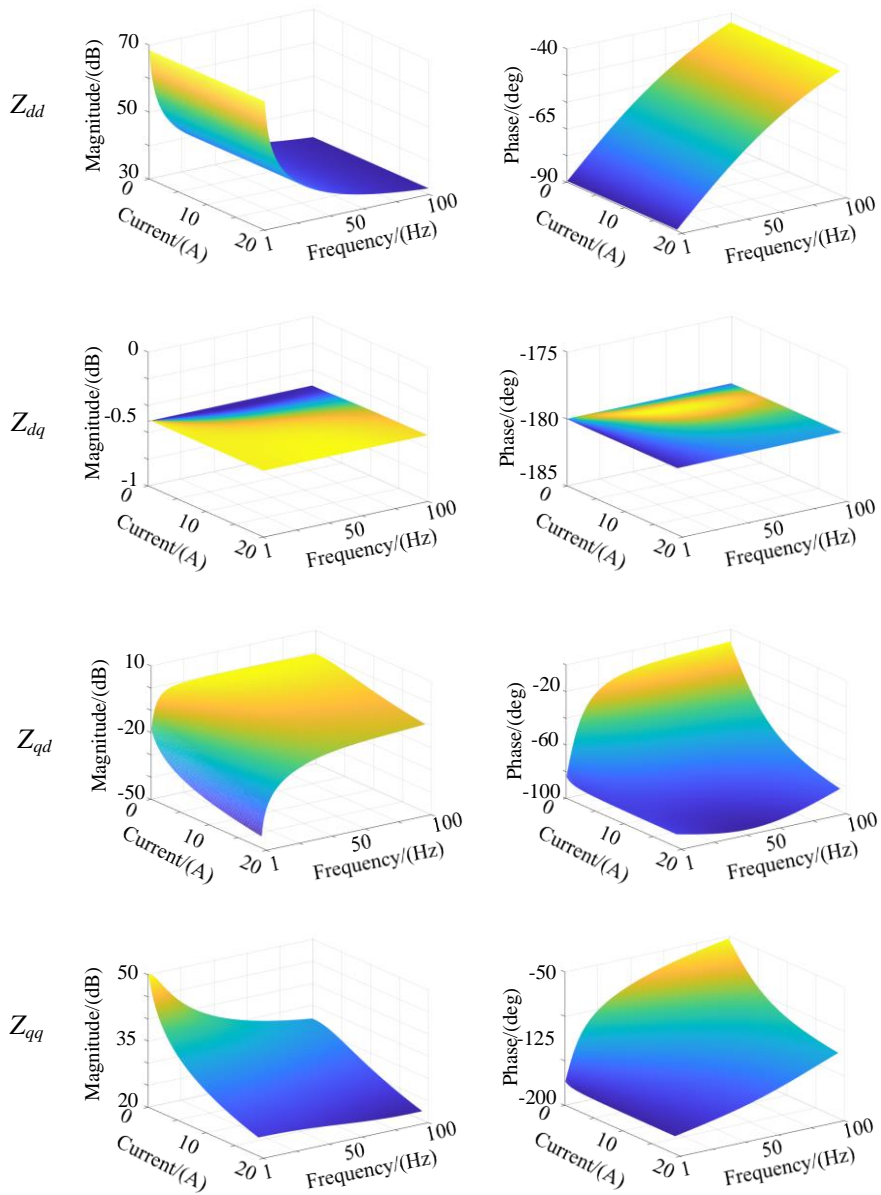$$Z_{gdq} = \begin{bmatrix} j2\pi f \cdot L_g & -2\pi f_0 \cdot L_g \\ 2\pi f_0 \cdot L_g & j2\pi f \cdot L_g \end{bmatrix} \tag{5.10}$$

where f_0 is the fundamental frequency. Thus, the impedance ratio at one operating point is show below

$$Le(j2\pi f) = Z_{gdq}(j2\pi f) \cdot Z_{inv}^{-1}(j2\pi f) \tag{5.11}$$

where $Z_{inv}(j2\pi f)$ is the impedance at the frequency f that is obtained with the MOP-impedance model generated above. Then calculate the eigenlocus of the system with the sweeping frequency in the following equation

$$\det\left[\lambda I - Le(j2\pi f)\right] = 0 \tag{5.12}$$

The stability state of a grid-connected VSC system at the specific operating point is predicted by analyzing the eigenlocus. By sweeping the operating point of the MOP-impedance model, the stability state at the global operating points is obtained. Then the stability state dataset is achieved.

The inputs of the dataset are the operating point, while the outputs are the stability state of the grid-VSC interaction system. Then the dataset is fed into the DNN shown in Figure 5-5 and the stability discrimination model is obtained.
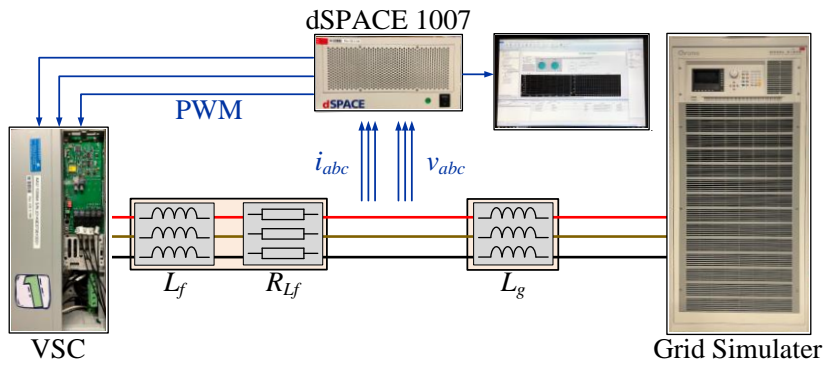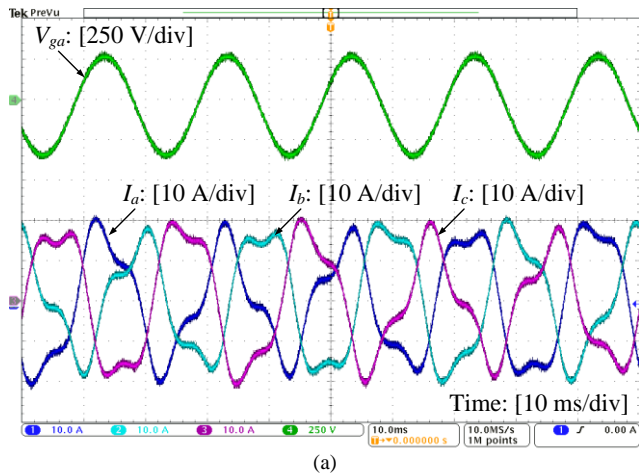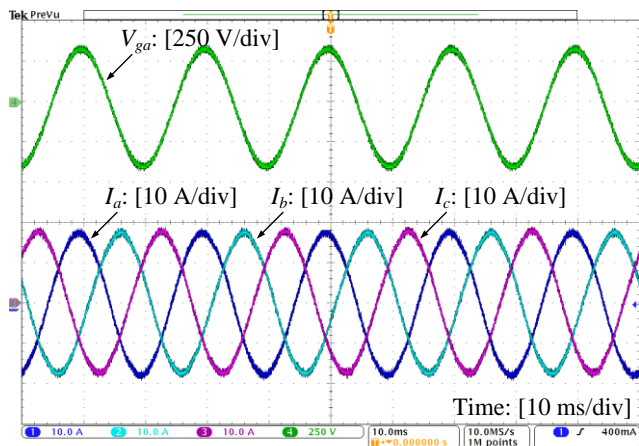
Figure 5-10. Experiment setup.

(a)

(b)
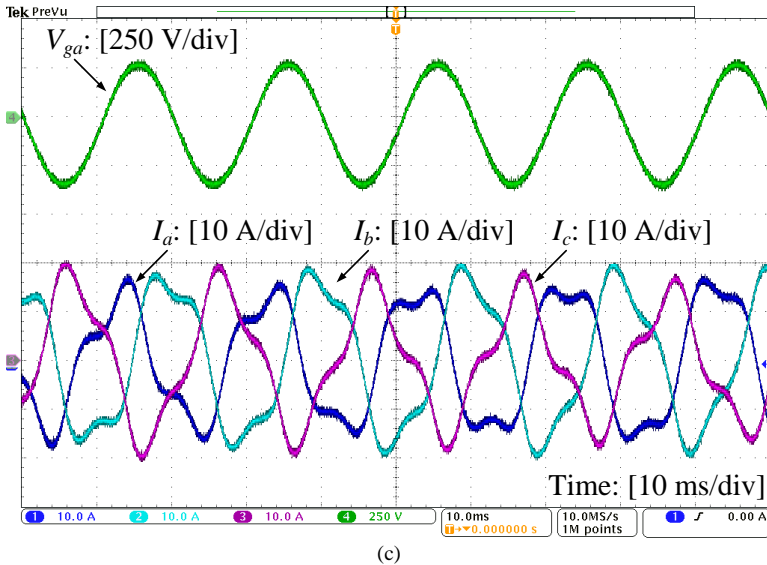
(c)
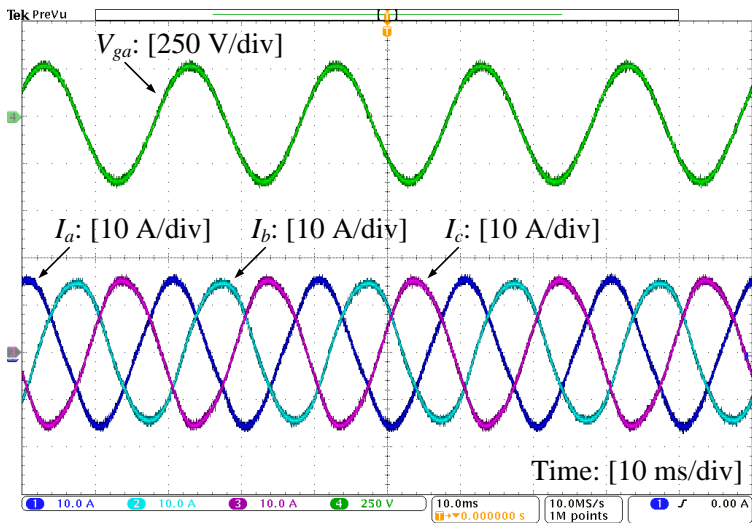
(d)

Figure 5-11. Experimental results of grid-connected VSC system at different operating points.
(a) Case I: operating point a, (b) Case II: operating point b, (c) Case III: operating point c,
(d) Case IV: operating point d.

Symbol	I_d	I_q	V_d	Stability
a	18 A	0 A	311 V	-
b	18 A	0 A	367 V	+
c	15 A	12 A	311 V	-
d	15 A	8 A	311 V	+

Table 5-3. Stability Prediction at Different Operating Points.

The experimental tests are carried out for the system shown in Figure 5-6. The experiment setup is shown in Figure 5-10. The dSPACE DS1007 is used to control the VSC. Four random operating points are sent into the model, the predicted stability conditions and the corresponding operating points are shown in Table 5-3, Figure 5-11 shows the corresponding experimental results, where the V_{ga} represents the grid voltage and I_a, I_b, I_c are the output current of VSC. The experimental results can show the utility of the proposed approach for stability estimation of the grid-converter system.

5.5.3. STABILITY REGION ESTIMATION AND ACCURACY ANALYSIS

The stability region can be estimated using the generated DNN-based stability discrimination model by sweeping the operating points. Figure 5-12 shows the stability region of the system. The blue region is the stability region and the yellow region denotes the unstable scenarios.
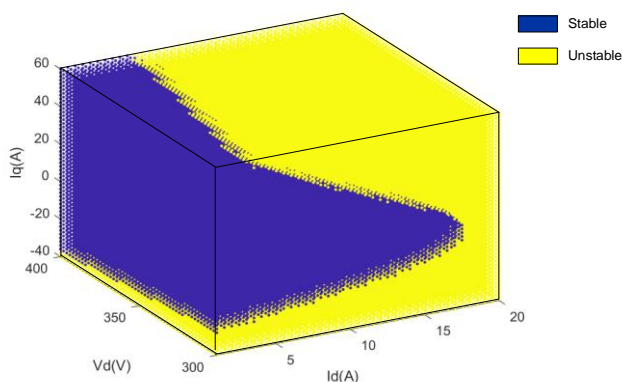
Figure 5-12. Stability region of the power-electronics-based power system.

N \ P	Stable	Unstable
Stable	197	4
Unstable	3	196

Figure 5-13. Confusion matrix of the stability estimation model.

Massive experiments with random 400 operating points are conducted. The confusion matrix of the model is shown in Figure 5-13, where P represents the actual stability results in the data and N represents the predicted stability results in the data. The accuracy of the model is 98.25 %, which can validate the accuracy of the model.

5.6. SUMMARY

This chapter has proposed a double DNN based black-box modeling and stability region estimation method for the grid-converter interaction system with the changing operating points, consisting of a DNN based MOP-impedance model and a DNN-based stability discrimination model. The stability region can be accurately generated by the proposed approach. The case study is conducted to demonstrate the utility of the method.

CHAPTER 6. CONCLUSION

6.1. CONCLUSION

The thesis investigates the modeling method for the stability analysis due to the wide integration of power electronics in modern power systems.

- To accurately model the VSCs considering the nonlinear part e.g., dead-time effect, the mechanism of VSC is analyzed considering the current ripple. The DIDF method is employed for nonlinear modeling. The presented impedance model could accurately help the stability analysis of the grid-converter system.

- An ANN-based impedance identification method is developed in the Ph.D. thesis to model the VSC at the changing operating points. A methodology adopting the ANN technique for the VSC modeling is illustrated. The designed case study is used to verify the superiority of the proposed method to existing methods.

- Considering the data limitation in online impedance measurement, a new impedance identification method using transfer learning for online impedance identification of VSC under changing operating points is proposed in the Ph.D. thesis. The partial physics of the VSC is used to compress the artificial neural network, which can reduce the calculation burden of online impedance identification. Meanwhile, the two-steps impedance identification is developed with the inspiration of the transfer learning theory to further increase the efficiency of the method. The proposed method can be used for online impedance identification and stability analysis effectively.

- To use the developed ANN-based impedance model for the stability analysis, a double DNN based black-box modeling and stability region estimation method is developed in the thesis for the grid-connected VSC system, consisting of a DNN based MOP-impedance model and a DNN-based stability discrimination model. The stability region of the grid-converter system can be accurately obtained with the proposed method.

6.2. FUTURE WORK AND IMPROVEMENT

There are still some open questions left unaddressed in this Ph.D. project, which are worth investigating in the future.

- In this thesis, only a single grid-tied converter system is discussed, the multi converter system will have more challenges. The future study should expand the proposed method in the multi converter power system, including different types of converters.

- The research about transfer learning based identification has the assumption that the control structure is known. If the control structure is not available, how to use the physical knowledge to accelerate the training process is a problem. The future research should make this method more scalable.

- It is meaningful to compare different machine learning methods in the impedance model identification and give an overview on it.

BIBLIOGRAPHY

[1] International Renewable Energy Agency (IRENA). Renewable capacity statistics 2020. 2020.

[2] J. Lee and F.Zhao. Global wind report 2019. 2020.

[3] J. Fang, H. Li, Y. Tang and F. Blaabjerg, "On the Inertia of Future More-Electronics Power Systems," *IEEE Journal of Emerging and Selected Topics in Power Electronics*, vol. 7, no. 4, pp. 2130-2146, Dec. 2019.

[4] U. Markovic, O. Stanojev, E. Vrettos et al. "Understanding small-signal stability of low-inertia systems," *IEEE Transactions on Power Systems*, doi:10.1109/TPWRS.2021.3061434.

[5] L .Ljung, T. Glad, "Modeling of Dynamic Systems", Prentice Hall, 1994.

[6] L. Ljung, "Perspectives on system identification", Annual Reviews in Control, vol. 34, no. 1, Ap. 2010, pp.1–12.

[7] Gabor Horvath, "Neural Networks for Instrumentation, Measurements and Related Industral applications,chapter 4", 2003, IOS Press, Nato Science Series.

[8] O. Nelles, "Nonlinear System Identification", 2001, Springer-Verlag.

[9] Torsten Bohlin, "Practical Grey-box process identification", 2006, Springer.

[10] M. M. Peretz and S. Ben-Yaakov, "Time domain identification of PWM converters for digital controller design", in *Proc. IEEE Power Electron. Spec. Conf.*, pp.809 -813 2007.

[11] F. Huerta, S. Cóbreces, F.J. Rodríguez, D. Pizarro, F.J. Meca, "Black-box identification for an auto-tuned current controller working with Voltage Source Converters connected to the grid through a LCL filter", in *Proc. of IEEE International Symposium on Industrial Electronics* (*ISIE*), 2010, pp. 96-101.

[12] B. Johansson and M. Lenells, "Possibilities of obtaining small-signal models of DC-to-DC power converters by means of system identification," in *Proc. Telecommunications Energy Conf.*, 2000, pp. 65–75.

[13] G. W. Wester, "Low-frequency characterization of switched dc-dc converters", PhD Thesis, 1972, California Institute of Technology, Pasadena.

[14] R. D Middlebrook, S. Cuk, "A general Unified Approach to Modeling Switching Converter Power Stage", in *Proc. IEEE Power Electron. Spec. Conf.*, 1976, pp 18-34.

[15] J. Sun, D. Mitchell, M. Greuel, P. Krein and R. Bass, "Averaged modeling of PWM converters operating in discontinuous conduction mode", *IEEE Trans. Power Electron.*, vol. 16, no. 4, pp.482 -492 2001.

[16] L. Harnefors, L. Zhang, and M. Bongiorno, "Frequency-domain passivity based current controller design," *IET Power Electron.*, vol. 1, no. 4, pp. 455–465, Dec. 2008.

[17] Y.Wang, X.Wang, F. Blaabjerg, and Z. Chen, "Harmonic instability assessment using state-space modeling and participation analysis in inverter-fed power systems," *IEEE Trans. Ind. Electron.*, vol. 64, no. 1, pp. 806–816, Jan. 2017.

[18] P. M. Anderson, B. L. Agrawal, and J. E. Van Ness, Subsynchronous Resonance in Power Systems. New York, NY, USA: IEEE Press, 1990.

[19] G. C. Verghese, I. J. Perezarriaga, and F. C. Schweppe, "Selective modal analysis with applications to electric power systems, part II: The dynamic stability problem," *IEEE Trans. Power App. Syst.*, vol. PAS-101, no. 9, pp. 3126–3134, Sep. 1982.

[20] X. Wang and F. Blaabjerg, "Harmonic stability in power electronic based power systems: Concept, modeling, and analysis," *IEEE Trans. Smart Grid*, vol. 10, no. 3, pp. 2858–2870, May 2019.

[21] J. Sun, "Impedance-Based Stability Criterion for Grid-Connected Inverters," IEEE Trans. Power Electron, vol. 26, no. 11, pp. 3075-3078, Nov. 2011..

[22] C. Zhang, M. Molinas, A. Rygg and X. Cai, "Impedance-Based Analysis of Interconnected Power Electronics Systems: Impedance Network Modeling and Comparative Studies of Stability Criteria," *IEEE Journal of Emerging and Selected Topics in Power Electronics*, vol. 8, no. 3, pp. 2520-2533, Sep. 2020.

[23] A. Rygg, M. Molinas, C. Zhang and X. Cai, "On the Equivalence and Impact on Stability of Impedance Modeling of Power Electronic Converters in Different Domains," *IEEE Journal of Emerging and Selected Topics in Power Electronics*, vol. 5, no. 4, pp. 1444-1454, Dec. 2017.

[24] M. K. Bakhshizadeh et al., "Couplings in phase domain impedance modelling of grid-connected converters," *IEEE Trans. Power Electron.*, vol. 31, no. 10, pp. 6792–6796, Oct. 2016.

[25] H. Zong, J. Lyu, C. Zhang, X. Cai, M. Molinas and F. Rao, "MIMO impedance based stability analysis of DFIG-based wind farm with MMC-HVDC in modifed

sequence domain," *8th Renewable Power Generation Conference (RPG 2019)*, 2019, pp. 1-7.

[26] F. Chierchie, E. E. Paolini and L. Stefanazzi, "Dead-Time Distortion Shaping," *IEEE Transactions on Power Electronics*, vol. 34, no. 1, pp. 53-63, Jan. 2019.

[27] L. Idkhajine, E. Monmasson and A. Maalouf, "AC drive system on chip controller with non-linearity errors compensation," 2008 34th Annual Conference of IEEE Industrial Electronics, Orlando, FL, 2008, pp. 2381-2386.

[28] Z. Zhang and L. Xu, "Dead-Time Compensation of Inverters Considering Snubber and Parasitic Capacitance," *IEEE Trans. Power Electron*, vol. 29, no. 6, pp. 3179-3187, June 2014.

[29] Yu Zhang, Xikun Chen, Yong Kang and Jian Chen, "The restrain of the dead time effects in parallel inverters," IEEE International Conference on Electric Machines and Drives, 2005., San Antonio, TX, 2005, pp. 797-802.

[30] S. Ahmed, Z. Shen, P. Mattavelli, D. Boroyevich and K. J. Karimi, "Small-Signal Model of Voltage Source Inverter (VSI) and Voltage Source Converter (VSC) Considering the DeadTime Effect and Space Vector Modulation Types," *IEEE Transactions on Power Electronics*, vol. 32, no. 6, pp. 4145-4156, June 2017.

[31] A. Rodriguez-Cabero, M. Prodanovic and J. Roldan-Perez, "Analysis of Dynamic Properties of VSCs Connected to Weak Grids including the Effects of Dead-Time and Time Delays," *IEEE Transactions on Sustainable Energy*., early access.

[32] Zhang, Qianjin, Lin Zhou, Mingxuan Mao, Bao Xie, and Chen Zheng, "Power quality and stability analysis of large-scale grid-connected photovoltaic system considering non-linear effects," *IET Power Electronics*, vol. 11, no. 11, pp. 1739-1747, May 2018.

[33] A. Mees and A. Bergen, "Describing functions revisited," *IEEE Transactions on Automatic Control*, vol. 20, no. 4, pp. 473-478, Aug. 1975.

[34] S. Shah et al., "Large-Signal Impedance-Based Modeling and Mitigation of Resonance of Converter-Grid Systems," *IEEE Trans. Sustain. Energy*, vol. 10, no. 3, pp. 1439–1449, July 2019.

[35] V. Valdivia et al., "Simple Modeling and Identification Procedures for 'Black-Box' Behavioral Modeling of Power Converters Based on Transient Response Analysis," *IEEE Trans. Power Electron*., vol. 24, no. 12, pp. 2776–2790, Dec. 2009.

[36] A. Francés, R. Asensi, and J. Uceda, "Blackbox Polytopic Model With Dynamic Weighting Functions for DC-DC Converters," *IEEE Access*, vol. 7, pp. 160263–160273, Nov. 2019.

[37] M. Cespedes and J. Sun, "Three-phase impedance measurement for system stability analysis," *2013 IEEE 14th Workshop on Control and Modeling for Power Electronics (COMPEL)*, Salt Lake City, UT, 2013, pp. 1-6.

[38] D. Zhang, D. Y. Chen, M. J. Nave, and D. Sable, "Measurement of noise source impedance of off-line converters," IEEE Trans. Power Electron., vol. 15, no. 5, pp. 820–825, Sep. 2000

[39] R.Y. Wang, D.M. Strong, and L.M. Guarascio, "Beyond Accuracy: What Data Quality Means to Data Consumers," (No. TDQM-94-10). Cambridge, Mass.: Total Data Quality Management Research Program, MIT Sloan School of Management, 1994.

[40] A. Guha and G. Narayanan, "Impact of Undercompensation and Overcompensation of Dead-Time Effect on Small-Signal Stability of Induction Motor Drive," *IEEE Transactions on Industry Applications*, vol. 54, no. 6, pp. 6027-6041, Nov.-Dec. 2018.

[41] H. Gong, D. Yang, and X. Wang, "Impact analysis and mitigation of synchronization dynamics for DQ impedance measurement," *IEEE Trans. Power Electron.*, vol. 34, no. 9, pp. 8797–8807, Sep. 2019.

[42] X. Wang, "Unified Impedance Model of Grid-Connected Voltage-Source Converters," *IEEE Trans. Power Electron.*, vol. 33, no. 2, pp. 1775–1787, Feb. 2018.

[43] H. Gong, D. Yang and X. Wang, "Impact of Nonlinear Dynamics on Converter DQ Impedance Measurement," in *Proc. Control and Modeling for Power Electronics (COMPEL)*, June 2019, pp. 1-6.

[44] B. Miao, R. Zane and D. Maksimovic, "System identification of power converters with digital control through cross-correlation methods," *IEEE Trans. Power Electron.*, vol. 20, no. 5, pp. 1093-1099, Sept. 2005.

[45] A. Riccobono, M. Mirz, and A. Monti, "Noninvasive online parametric identification of three-phase AC power impedances to assess the stability of grid-tied power electronic inverters in LV networks," *IEEE J. Emerg.Sel. Top. Power Electron.*, vol. 6, no. 2, pp. 629-647, June 2018.

[46] A. Riccobono, E. Liegmann, M. Pau, F. Ponci and A. Monti, "Online parametric identification of power impedances to improve stability and accuracy of power

hardware-in-the-loop simulations," *IEEE Trans. Instrum. Meas.*, vol. 66, no. 9, pp. 2247-2257, Sept. 2017.

[47] Z. Shen, M.Jaksic, B.Zhou, P.Mattavelli, J.Verhulst, M.Belkhayat, "Analysis of Phase Locked Loop (PLL) influence on DQ impedance measurement in three-phase AC systems," in *Proc. Appl. Power Electron. Conf. Expo.*, Mar. 2013, pp. 939–945.

[48] J. Schmidhuber, "Deep learning in neural networks: An overview," *Neural Netw.*, vol. 61, pp. 85–117, Jan. 2015.

[49] R. P. Lippmann, "An introduction to computing with neural nets," *IEEE ASSP Magazine*, pp. 3-22, Apr. 1987.

[50] P. Ramachandran, B. Zoph, and Q. V. Le, "Searching for activation functions," 2017, *arXiv: 1710.05941*. [Online]. Available: https://arxiv.org/abs/1710.05941.

[51] L. Bottou, "Large-scale machine learning with stochastic gradient descent," in *Proc. 19th Int. Conf. Comput. Statist.*, pp. 177–186, Sept. 2010.

[52] S. S. Du, X. Zhai, B. Poczos, and A. Singh, "Gradient descent provably optimizes over-parameterized neural networks," 2018, *arXiv: 1810.02054*. [Online]. Available: https://arxiv.org/abs/1810.02054.

[53] S. J. Pan and Q. Yang, "A Survey on Transfer Learning," *IEEE Trans. Knowl. Data Eng.*, vol. 22, no. 10, pp. 1345-1359, Oct. 2010.

[54] D. Pan, X. Ruan, C. Bao, W. Li, and X. Wang, "Optimized controller design for LCL-type grid-connected inverter to achieve high robustness against grid-impedance variation," *IEEE Trans. Ind. Electron*., vol. 62, no. 3, pp. 1537–1547, Mar. 2015.

[55] L. Harnefors, M. Bongiorno, and S. Lundberg, "Input-admittance calculation and shaping for controlled voltage-source converters*," IEEE Trans. Ind. Electron*., vol. 54, no. 6, pp. 3323–3334, Dec. 2007.

[56] Y. Qiu, H. Wu, Y. Zhou, and Y. Song, "Global parametric polynomial approximation of static voltage stability region boundaries," I*EEE Trans. Power Syst*., vol. 32, no. 3, pp. 2362–2371, May 2017.

[57] J. Schmidhuber, "Deep learning in neural networks: An overview," Neural Netw., vol. 61, pp. 85–117, Jan. 2015.

[58] G. Thimm and E. Fiesler, "Neural network initialization," in From Neural to Artificial Neural Computation. Berlin, Germany: Springer-Verlag, 1995, vol. 930, pp.

535–542, DOI: 10.1007/3- 540-59497-3_220, ISSN: 0302-9743, ISBN: 978-3-540-59497.

[59] Y. Chen and F. Bastani, "ANN with two-dendrite neurons and its weight initialization," in *Proc. Int. Joint Conf. Neural Netw.*, Baltimore, MD, Jun. 1992, pp. 139–1.

[60] Z.-H. Zhou and M. Li, "Semi-supervised regression with cotraining-style algorithms," *IEEE Trans. Knowl. Data Eng.*, vol. 19, no. 11, pp. 1479–1493, Nov. 2007.

[61] G. Hinton, N. Srivastava, and K. Swersky. (2012). Neural Networks for Machine Learning—Lecture 6a Overview of Mini-Batch Gradient Descent. Accessed: Mar. 20, 2018. [Online]. Available: https://www.cs. toronto.edu/~tijmen/csc321/slides/lecture_slides_lec6.pdf.

[62] A. MacFarlane and I. Postlethwaite, "The generalized Nyquist stability criterion and multivariable root loci," Int. J. Control, vol. 25, pp. 81–127, Jan. 1977.

[63] A. F. T. Martins and R. F. Astudillo, "From softmax to sparsemax: A sparse model of attention and multi-label classification," in *Proc. 33rd Int. Conf. Mach. Learn.*, vol. 48, 2016, p. 10.

[64] D. E. Rumelhart, G. E. Hinton, and R. J. Williams, "Learning representations by back-propagating errors," *Nature*, vol. 323, no. 6088, pp. 533–536, 1986.